Skoltech

Skolkovo Institute of Science and Technology

MASTER'S THESIS

Josephson junctions based on magnetic topological insulators

Master's Educational Program: Photonics and Quantum materials

Student_____

Andrei Kudriashov

Research Advisor:_____

Albert Nasibulin

Professor, Skolkovo Institute of Science and Technology, Center for Photonics and Quantum Materials

Co-Advisor:_____

Dr Vasily S. Stolyarov

Leading Research Scientist and d/Head of Topological Quantum Phenomena in Superconducting Systems Lab (TQPSS), Moscow Institute of Physics and Technology and Head of Superconducting and Quantum Technology Lab (SQT), Dukhov Research Institute of Automatics – VNIIA (ROSATOM Corporation)

Moscow 2021

Skoltech

Skolkovo Institute of Science and Technology

МАГИСТЕРСКАЯ ДИССЕРТАЦИЯ

Джозефсоновские контакты на основе магнитных топологических изоляторов

Магистерская образовательная программа: Фотоника и квантовые материалы

Студент_____

Андрей Кудряшов

Научный руководитель:_____

Альберт Насибулин

Профессор, Сколковский Институт Науки и Технологий, Центр фотоники и квантовых материалов

Со-руководитель:_____

Василий Столяров

Ведущий научный сотрудник, зам. заведующего лабораторией топологических квантовых явлений в сверхпроводящих системах, МФТИ, заведующий лабораторией сверхпроводящих квантовых технологий, ВНИИА им.Н.Л.Духова (РОСАТОМ)

Москва 2021

Josephson junctions based on magnetic topological insulators

Andrei Kudriashov

Submitted to the Skolkovo Institute of Science and Technology
on June 16, 2021

Abstract

The electronic band structure is significant to explain a lot of physical phenomena in condensed matter systems. The non-triviality of the band structure of some materials leads to the formation of new states of matter, such as topological insulators, Dirac or Weyl semimetals, and topological superconductors. In the frame of this work, the local electronic properties of novel material Fe-BSTS (iron-doped $BiSbTe_2Se$) have been studied by Scanning Tunnelling Microscopy (STM) and Spectroscopy (STS) and also by Angle-Resolved Photo Emission Spectroscopy (ARPES). It was demonstrated that the Fermi energy position inside the bulk bandgap makes this material a real bulk insulator. In addition, the signatures of the magnetic gap were observed by STS. Still, independent ARPES measurement did not resolve any magnetic gap near the Dirac point in the surface states, probably due to the inhomogeneous distribution of the iron atoms, which is supported by observing the defect clusters on the surface by STM. Also, we have demonstrated the ballistic Josephson effect on this material. Based on this material, the dc-SQUID shows very pronounced oscillations of critical current with an external magnetic field. Critical current drops to zero due to the fact that supercurrent is flowing through only a few coherent ballistic channels. Another feature was observed is the double-critical current. We believe that the second critical current originates from the region underneath the Nb leads formed during Ar plasma etching and Nb deposition.

Research Advisor:
Name: Albert Nasibulin
Degree: Doctor of Sciences
Title: Professor, Skolkovo Institute of Science and Technology, Center for Photonics and Quantum Materials

Co-Advisor:
Name: Dr Vasily S. Stolyarov
Degree: PhD
Title: Leading Research Scientist and d/Head of Topological Quantum Phenomena in Superconducting Systems Lab (TQPSS), Moscow Institute of Physics and Technology and Head of Superconducting and Quantum Technology Lab (SQT), Dukhov Research Institute of Automatics – VNIIA (ROSATOM Corporation)

Джозефсоновские контакты на основе магнитных топологических изоляторов

Андрей Кудряшов

Представлено в Сколковский институт науки и технологий
Июнь 16, 2021

Реферат

Электронная зонная структура важна для объяснения многих физических явлений физики твердого тела. Нетривиальность зонной структуры некоторых материалов приводит к образованию новых состояний вещества, таких как топологические изоляторы, полуметаллы Дирака и Вейля или топологические сверхпроводники. В рамках исследовательской работы локальные электронные свойства нового материала Fe-BSTS (легированный железом $BiSbTe_2Se$) были изучены методами сканирующей туннельной микроскопии (СТМ) и спектроскопии (СТС) и также с помощью фотоэмиссионной спектроскопии с угловым разрешением (ARPES). Было продемонстрировано, что энергетическое положение уровня Ферми внутри объемной запрещенной зоны делает этот материал настоящим объемным изолятором. Кроме того, признаки присутствующей магнитной щели были обнаружены при помощи STS. Тем не менее, независимое измерение ARPES не позволило выявить магнитную щель вблизи точки Дирака в поверхностных состояниях, вероятно, из-за неоднородного распределения атомов железа, что подтверждается наблюдением кластеров дефектов на поверхности с помощью СТМ. Также мы демонстрируем баллистический эффект Джозефсона на этом материале. Реализованный на этом материале СКВИД на постоянном токе демонстрирует очень выраженные колебания критического тока в зависимости от внешнего магнитного поля. Критический ток падает до нуля из-за того, что сверхток протекает только через несколько когерентных баллистических каналов. Обнаружена еще одна особенность - второй критический ток. Мы полагаем, что второй критический ток локализован в областях под контактами Nb, образовавшихся в процессе плазменного травления ионами Ar и осаждения Nb.

Научный руководитель:
Имя: Альберт Насибулин
Ученое звание, степень: Доктор физико-математических наук
Должность: Профессор, Сколковский Институт Науки и Технологий, Центр фотоники и квантовых материалов

Со-руководитель:
Имя: Василий Столяров
Ученое звание, степень: Кандидат физико-математических наук
Должность: Ведущий научный сотрудник, зам. заведующего лабораторией топологических квантовых явлений в сверхпроводящих системах, МФТИ, заведующий лабораторией сверхпроводящих квантовых технологий, ВНИИА им.Н.Л.Духова (РОСАТОМ)

Acknowledgments

I would like to express my very profound gratitude to my scientific supervisor Dr. Vasily S. Stolyarov for the wise guidance in scientific and life issues, which helped me to become not only a better scientist but also a better person.

I would like to thank Rikizo Yano, Hishiro Hirose, Taiki Tsuda, Hiromi Kashiwaya, Takao Sasagawa and Satoshi Kashiwaya for providing bulk crystals of magnetic topological insulators; Denis Vyalikh and Aleksandr Fedorov for conducting an angle-resolved photoemission spectroscopy; Professor Alexander Golubov for the help with theoretical analysis of the experimental results and useful discussions, Professor Jukka Pekola for providing Coulomb blockade thermometer for the help with electronic temperature measurement.

I am very grateful to the other researchers from the Laboratory of Topological Quantum Phenomena in Superconducting Systems in MIPT: to Andrey Shishkin for the help with the device fabrication; to Sergey Dizhur for the help with engineering work. Also, I would like to thank other members of the lab for all small and big assistance during the first steps in my scientific career.

I am also thankful to Professor Albert Nasibulin for recommendations on the presentation of results and valuable comments.

This study was supported by the Grant RSF-ANR 20-42-09033.

Thesis publications

1. Rikizo Yano, Andrei Kudriashov, Hishiro T. Hirose, Taiki Tsuda, Hiromi Kashiwaya, Takao Sasagawa, Alexander A. Golubov, Vasily S. Stolyarov, and Satoshi Kashiwaya, Magnetic Gap of Fe-Doped $BiSbTe_2Se$ Bulk Single Crystals Detected by Tunneling Spectroscopy and Gate-Controlled Transports, J. Phys. Chem. Lett., 12, 4180–4186 (2021).

Conferences

1. А.В. Кудряшов, А.Г. Шишкин, В.С. Столяров, Исследование сверхпроводящих гибридных структур на основе магнитных топологических изоляторов, 63-я Всероссийская научная конференция МФТИ, Москва, Россия.

2. А.В. Кудряшов, R. Yano, S. Kashiwaya, В.С. Столяров, Сканирующая туннельная спектроскопия магнитного топологического изолятора Fe – $BiSbTe_2Se$, 15 Международный симпозиум «Нанофизика и наноэлектроника», Нижний Новгород, Россия.

3. X. Song, A. Kudriashov, Y. Bai, G. Yue, S. Dizhur, S. Kozlov, E. Huemiller, D. J. Van Harlingen, J. N. Eckstein, V. Stolyarov, and A. Bezryadin, Critical current and magnetic interference effects in topological superconducting arrays of Nb islands coupled through Bi_2Se_3 epitaxial films, The 18^{th} International Vortex Workshop 2021, online.

Contents

Chapter 1
Introduction

Recently it has been recognized that the band topology is very important in order to explain a lot of physical phenomena in condensed matter systems. The non-triviality of the band structure of some materials leads to the formation of new states of matter, such as topological insulators, Dirac or Weyl semimetals, and topological superconductors. The existence of topological superconductors is not experimentally verified yet, but they would have very promising applications. Owing to their bulk band topology, topological superconductors have Majorana fermions on the boundaries of the material. It was predicted that such a condensed matter realization of Majoranas can be used to construct a fault-tolerant topological quantum computer, which is stable against local sources of decoherence. Topological superconductivity can be obtained via proximity effect between a trivial superconductor and a topological insulator.

One approach to topological quantum computation is braiding of non-Abelian zero-dimensional Majorana modes (the edges of a nanowire, the core of vortices, and so on). An alternative approach to topological quantum computation is using 1D Chiral Majorana fermions (CMF) instead of 0D Majorana modes. To create CMF we need to create a hybrid structure of magnetic topological insulator thin film and trivial superconductor. Proximity-induced superconductivity on the surface of a magnetic topological insulators is a key ingredient for studying Majorana physics. So, the goal of this work is to study the proximity effect between trivial superconductor (Nb) and the surface states of magnetic topological insulator (Fe – $BiSbTe_2Se$).

In the chapter "Background" we discuss the nature of Topological Insulators, Magnetic Topological Insulators, and Superconductors: theoretical predictions and history of experimental verification. Additionally, we describe previous works of our collaborators from Nagoya University, who have been synthesized crystals under study and performed some studies of their properties.

In the chapter "Technological and Experimental Methods" we describe details of the devices fabrication procedure and the methods, which were used in this work.

In the chapter "Results and Discussions" we present and analyze our experimental results. Firstly we perform Scanning Tunneling Microscopy and Angle-Resolved Photoemission Spectroscopy of bulk crystals. Further, we explore the transport properties of SQUID based on magnetic topological insulator Fe – $BiSbTe_2Se$.

And in the final chapter, we sup um results of the performed study.

Chapter 2

Background

The importance of global band topology is recognized in condensed matter physics. A lot of new states of matter, such as topological insulators, Dirac or Weyl semimetals, and topological superconductors have been discovered. This chapter is devoted to the discussion of the basic concepts of Topological Insulators, Magnetic Topological Insulators, and Superconductors and their experimental realization, together with the discovery and verification of their electronic properties. Additionally, previous works of our collaborators from Nagoya University, who have been synthesized crystals under study and performed some studies of their properties, are described.

2.1 3D Topological Insulators

It was theoretically predicted [1], that Bi_2Te_3, Bi_2Se_3 and Sb_2Te_3 are 3D time reversal invariant topological insulators. These materials share the same rhombohedral crystal struc-

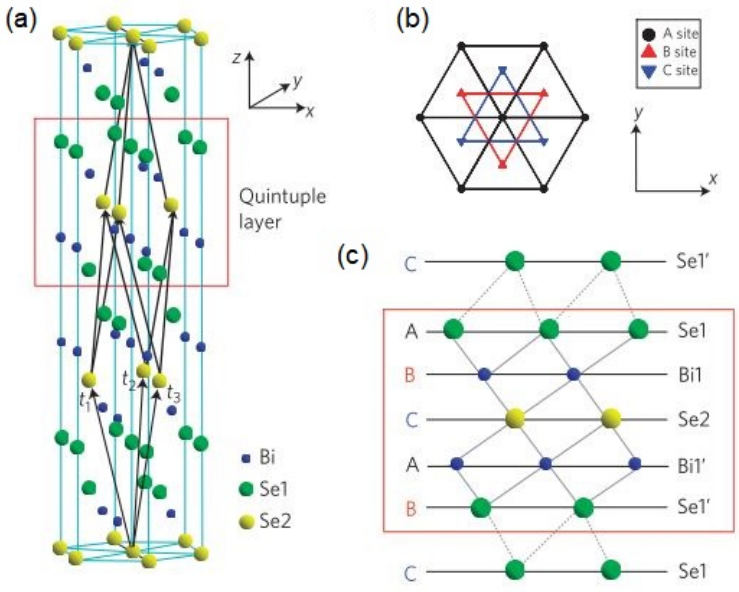

Figure 2.1: (a) The sketch of the lattice of Bi_2Se_3. $t_{1,2,3}$ are the primitive lattice vectors. The red square is a quintuple layer of the material. (b) The crystal structure from the top view. (c) Side view of the quintuple layer structure. The figure is adopted from [1].

ture ($R\bar{3}m$ space group), five atoms in the unit cell. The crystal structure of Bi_2Se_3 is shown in Fig.2.1(a). It has layered structures with a triangle lattice within one layer (see Fig.2.1(b)).

It has three-fold rotation symmetry (along the z-axis), two-fold rotation symmetry (along the x-axis), and the y-axis is a bisectrix axis. The crystal structure consists of layers, which are called quintuple layers. Quintuple layer consists of five atoms: two equivalent Se atoms (Se1 and Se1' in Fig.2.1(c)), two equivalent Bi atoms (Bi1 and Bi1' in Fig.2.1(c)) and a third Se atom (Se2 in Fig.2.1(c)). The coupling is strong between two atomic layers within one quintuple layer, but weak van der Waals between two quintuple layers. The primitive lattice vectors $t_{1,2,3}$ and rhombohedral unit cells are shown in Fig.2.1(a). The Se2 site is an inversion center. The existence of inversion symmetry let us to construct eigenstates of the Hamiltonian of that system with definite parity.

Due to the strong spin-orbit coupling (SOC), the bulk valence band and bulk conduction band are inverted. To get a better understanding of the inversion and the parity exchange, let's see the atomic energy levels and consider the effect of crystal-field splitting and SOC on the energy eigenvalues at the Γ point. This is summarized schematically in three stages (I), (II) and (III) in Fig.2.2(a). If the SOC is large enough ($\lambda > \lambda_c$), the order of $|P1_z^+\rangle$ and $|P2_z^-\rangle$ levels are reversed. This inversion process is sown in Fig.2.2(b) explicitly. As seen, a level crossing occurs between $|P1_z^+\rangle$ and $|P2_z^-\rangle$ energy levels when the SOC is about 60% of the realistic value (value in the real materials). Since these two levels have opposite parity, the inversion between them drives the system into a topological insulator phase. So, the mechanism for the 3D topological insulator in this system is exactly the same as in the 2D topological insulator HgTe.

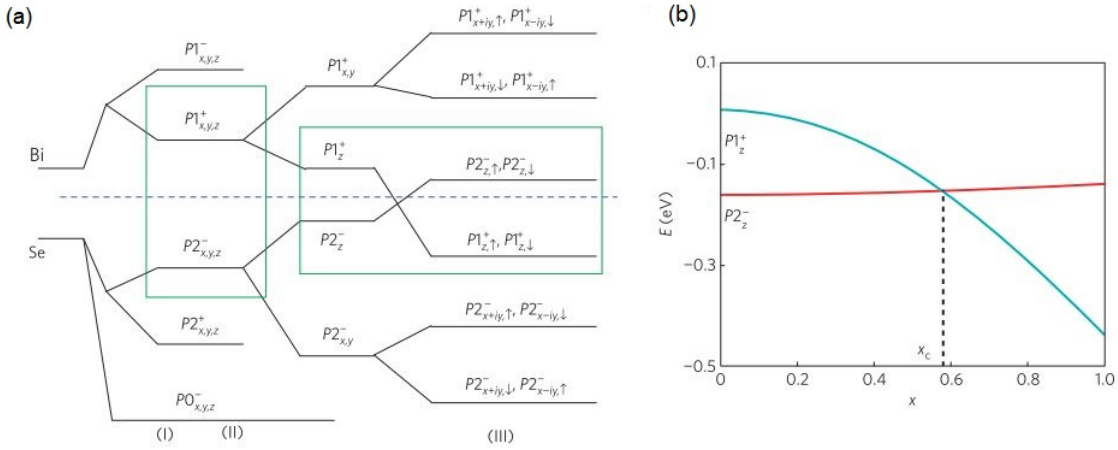

Figure 2.2: (a) Schematic diagram of the evolution from the atomic $p_{x,y,z}$ orbitals of Bi and Se into the conduction and valence bands of Bi_2Se_3 at the Γ point. The three different stages (I), (II) and (III) represent the effect of turning on chemical bonding, crystal-field splitting and spin-orbit coupling, respectively. The blue dashed line represents the Fermi energy. (b) The energy levels $|P1_z^+\rangle$ and $|P2_z^-\rangle$ of Bi_2Se_3 at the Γ point versus an artificially rescaled atomic SOC $\lambda(Bi) = x\lambda_0(Bi) = 1.25x$ eV, $\lambda(Se) = x\lambda_0(Se) = 0.22x$ eV. A level crossing occurs between these two states at $x = x_c \approx 0.6$. Figure is adopted from [1].

The topological nature of insulators is determined by the physics near the Γ point, so it is possible to write down a simple effective Hamiltonian to characterize the low-energy properties of the system. Starting from the four low-lying states $|P1_z^+, \uparrow (\downarrow)\rangle$ and $|P2_z^-, \uparrow (\downarrow)\rangle$

at the Γ point, such a Hamiltonian can be constructed by the theory of invariants for the finite wave vector $\mathbf{k}$. On the basis of the symmetries of the system, the generic form of the 4×4 effective Hamiltonian can be written down up to the order of $O(\mathbf{k}^2)$, and the tunable parameters in the Hamiltonian can be obtained by fitting the band structure of *ab initio* calculation. The important symmetries of the system are time-reversal symmetry T, inversion symmetry I, and three-fold rotation symmetry $C3$ along the z axis. By requiring these three symmetries and keeping only the terms up to quadratic order in $\mathbf{k}$, one can obtain the following generic form of the effective Hamiltonian:

$$H(\mathbf{k}) = \epsilon_0(\mathbf{k})I_{4x4} + \begin{pmatrix} M(\mathbf{k}) & A_1k_z & 0 & A_2k_- \\ A_1k_z & -M(\mathbf{k}) & A_2k_- & 0 \\ 0 & A_2k_+ & M(\mathbf{k}) & -A_1k_z \\ A_2k_+ & 0 & -A_1k_z & -M(\mathbf{k}) \end{pmatrix} + o(\mathbf{k}^2), \tag{2.1}$$

where $\mathbf{k} = (k_x, k_y, k_z)$ is a wave vector, $\epsilon_0(\mathbf{k}) = C + D_1k_z^2 + D_2k_\perp^2$, A_1, A_2, C, D_1, D_2, M are material parameters, $k_- = k_x - ik_y$, $k_+ = k_x + ik_y$, $k_\perp = \mathbf{k} \cdot \mathbf{e}_z$.

As a consequence of the nontrivial band structure at the interface between a topological insulator and a trivial insulator (or vacuum), topologically protected conducting states with a linear dispersion and spin-momentum locking should exist. Generally speaking, there are always a gapless states at the interface between topologically distinct insulators (insulators with different topological invariants). This is called bulk-boundary correspondence. The Hamiltonian for topological surface states can be obtained from diagonalizing the effective Hamiltonian equation 2.1 with an open boundary condition. For a surface perpendicular to the z-direction (that is, the [111] direction), k_x, k_y are still good quantum numbers but k_z is not. By substituting $-i\partial z$ for k_z in equation 2.1, one can write down the 1D Schrodinger equations for the wavefunctions $\Psi_{k_x,k_y}(z)$. For $k_x = k_y = 0$, there are two renormalizable surface-state solutions on the half infinite space $z > 0$, denoted by $|\Psi_{0\uparrow}\rangle$, $|\Psi_{0\downarrow}\rangle$. By projecting the bulk Hamiltonian 2.1 onto the subspace of these two surface states, to the leading order of k_x, k_y we obtain the following surface Hamiltonian:

$$H_{surf}(k_x, k_y) = \hbar v_F \begin{pmatrix} 0 & k_x + ik_y \\ k_x + ik_y & 0, \end{pmatrix}, \tag{2.2}$$

where v_F is the Fermi velocity and $\hbar$ is a reduced Planck constant.

This result is supported by DFT calculations. Local density of states as a function of energy and momentum is presented in Fig.2.3. It is clearly seen, that Sb_2Se_3 does not have surface states inside the bulk band gap (it is trivial insulator), but Bi_2Se_3, Bi_2Te_3 and Sb_2Te_3 have states in the bulk band gap (they are topological insulators). I would like to note the position of Dirac point: in Bi_2Se_3 and Sb_2Te_3 the Dirac point is located above the bulk valence band, but Bi_2Te_3 has Dirac point below the bulk valence band. This is important when we brake time-reversal symmetry (for details see the next paragraph). Also, in the

ideal situation of infinite periodic structure without defects Fermi energy is located in the Dirac point (for Bi_2Se_3 and Sb_2Te_3) and at the top of the valence band (for Bi_2Te_3). This result let us to conclude that Bi_2Se_3 is an ideal platform for observing different phenomena, related to topological properties because it has big band gap of approximately 0.4 meV and the Dirac point is located in the bulk band gap. The existence of surface states with linear

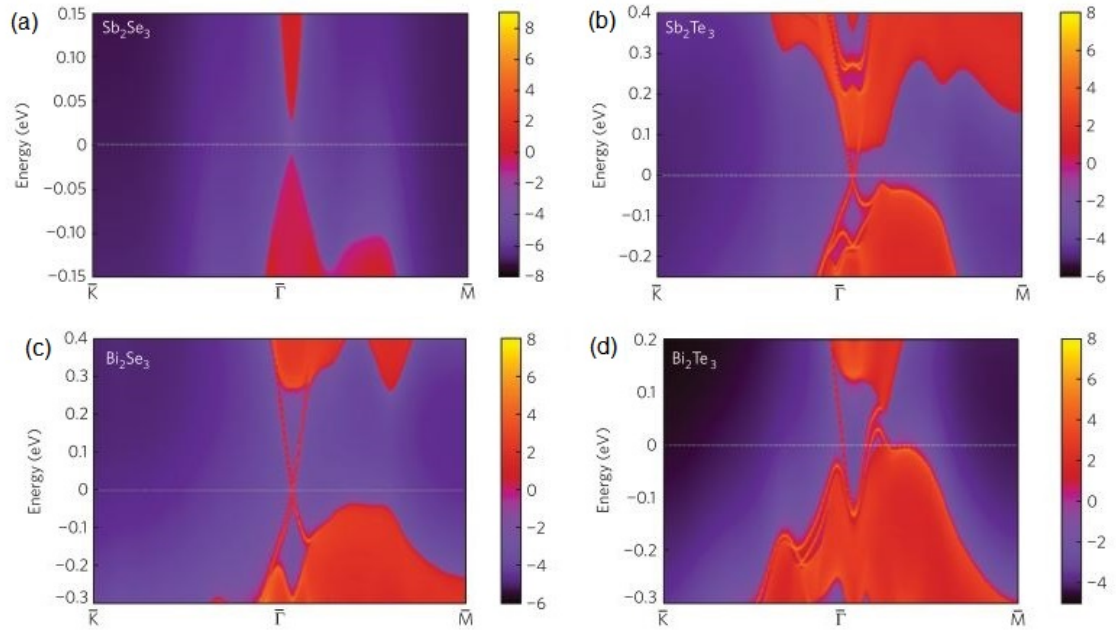

Figure 2.3: Energy and momentum dependence of the LDOS for Sb_2Se_3 (a), Sb_2Te_3 (b), Bi_2Se_3 (c) and Bi_2Te_3 (d) on the [111] surface. Figure is adopted from [1].

dispersion relation has been confirmed in many experiments (see, for example, [2]). Fig.2.4 demonstrate ARPES measurements of spectrum for Bi_2Se_3 and Bi_2Te_3. The linear dispersion is clearly seen and the position of the Dirac point is consistent with the DFT calculations.

These works opened a new era in the study of 3D TRI TI, since these materials are the first discovered strong topological insulators with a very simple structure of surface states (only one Dirac cone). However, as one can see from ARPES measurements, Fermi energy is located in the conduction band. With the growth of these crystals, a large number of selenium or tellurium vacancies are formed, which leads to a shift of the chemical potential (see Fig.2.4). As a consequence, real materials are not bulk insulators, but exhibit metallic conductivity, which complicates or even makes it impossible to observe transport effects associated with surface states. One way to overcome this problem is to begin to synthesize and study nonstoichiometric three-component materials such as $Bi_2(Te,Se)_3$ or $(Bi,Sb)_2Te_3$ or similar. It is possible to optimize the growth in such a way, that Fermi level is located inside the bulk band gap. As a consequence, these materials demonstrate predominantly surface conductivity at temperatures below 25 K and crystal thicknesses up to 120 nm [3], while on binary compounds it is possible to reduce the contribution of bulk carriers only in thin films (a few nanometers) and cooling sample down below 1 K. Fig.2.5(a) shows semiconducting-like behaviour at high temperature in bulk Bi_2Te_2Se crystal. Arrhenius analysis (Fig.2.5(b))

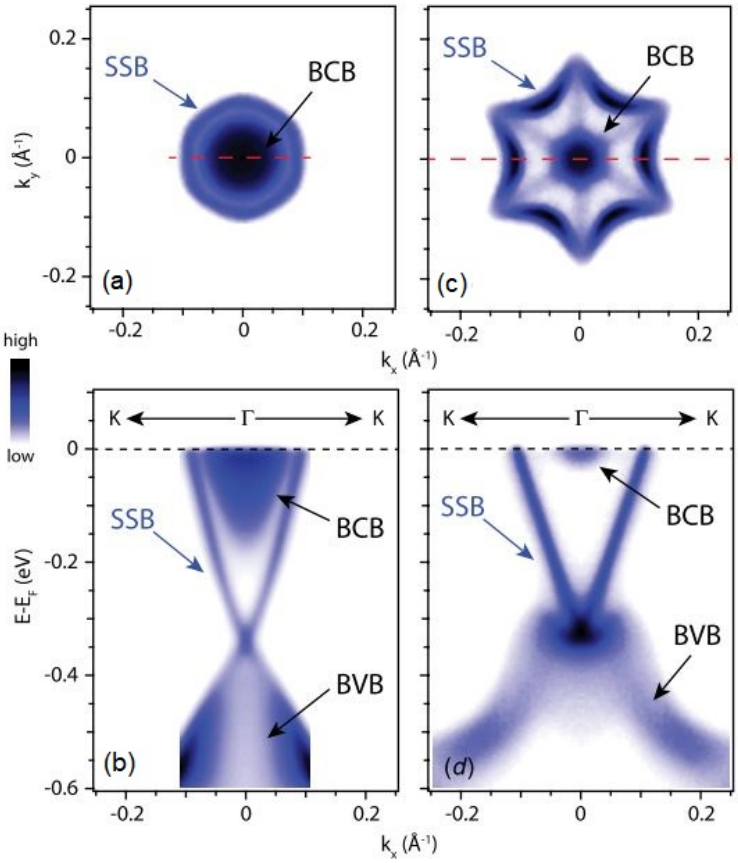

Figure 2.4: Electronic structure of Bi_2Se_3 and Bi_2Te_3 measured by ARPES. (a) Fermi surface map and (b) band structure plot along high symmetry cut $\Gamma - K$ (indicated by the red dashed line in panel (a)) of Bi_2Se_3.(c) and (d) are the corresponding plots of Bi_2Te_3. Different types of bands are labeled as surface state band (SSB), bulk conduction band (BCB), and bulk valence band (BVB). Figure is adopted from [2].

shows the value of activation energy of 28.1 meV, but the resistance reaches its maximum point at 20 K and then start to decreases, indicating metallic-like behaviour. One of the main features of the topological surface state in transport is weak anti localization (WAL) effect. The response of the conductance to the magnetic field in a 2D system with WAL can be described by a well-known Hikami-Larkin-Nagaoka model:

$$\Delta G_{2D} = \alpha \frac{e^2}{2\pi h}[\Psi(\frac{1}{2} + \frac{B_\phi}{B}) - ln(\frac{B_\phi}{B})] - cB^2, \tag{2.3}$$

where ΔG_{2D} is a change in conductance of 2D material, Ψ is digamma function, B is a magnetic field, $B_\phi = \hbar/(4eL_\phi^2)$ and L_ϕ is a coherence length.

In this work Shekhar and collaborators have observed WAL (see Fig.2.5(c)), prooving surface dominated transport in their material at temperatures smaller than 20 K.

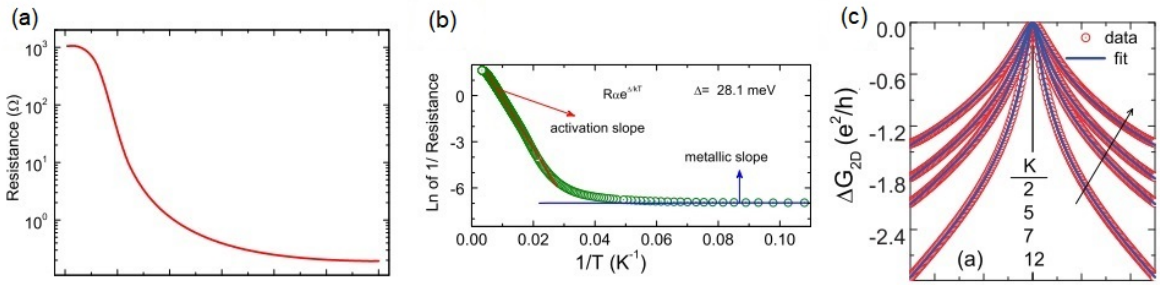

Figure 2.5: (a) Temperature dependence of resistance of the bulk single crystal of Bi_2Te_2Se. (b) Arrhenius analysis of R(T). The resistance follows $R = R_0 e^{\Delta/k_B T}$ in the temperature range down to 30 K as indicated by the red line; at lower temperatures it follows metallic behavior, which is indicated by the blue line. (c) Magnetoresistance at different temperatures, demonstarting WAL effect. Figure is adopted from [3].

2.2 Magnetic Topological Insulators

It has been theoretically shown (see, for example, [4]) that the induction of ferromagnetism in these materials leads to the opening of a gap in the spectrum of surface states, because the conduction electrons couple with the magnetization via an exchange interaction, as described by the model Hamiltonian:

$$H = \hbar v_F (k_x \sigma_y - k_y \sigma_x) + m\sigma_z, \tag{2.4}$$

where m is an exchange interaction, $\sigma_{x,y}$ are Pauli matrices in the space of real spin of electrons.

Part of Hamiltonian, which is proportional to σ_z breaks time-reversal symmetry, because it does not commute with the time-reversal operator $T = -i\sigma_y K$, where K is a complex conjugation.

This prediction has been confirmed in many experiments. For example, in [5] Chen and collaborators have shown the opening of a magnetic gap in iron-doped Bi_2Se_3 crystals using ARPES. Results are shown in Fig.2.6. As one can see, introducing nonmagnetic dopants (Tl) up to 10% does not destroy Dirac point. So, surface states are robust against nonmagnetic perturbations. But if we introduce magnetic dopants (Fe in this case) up to the same concentration, visible gap of about 30 meV appears in the surface state.

If the Fermi level is located in the magnetic gap, we do not have metallic surface state anymore, but we have 2D insulator. This is called 2D Chern insulator. In tat case, Chern number plays a role of topological invariant, reflecting topological properties of 2D insulator:

$$C = 2\int_{BZ} \hat{\mathbf{R}}\left(\frac{\partial \hat{\mathbf{R}}}{\partial k_x} \times \frac{\partial \hat{\mathbf{R}}}{\partial k_y}\right)\frac{dk_x dk_y}{4\pi} = sgn(m), \tag{2.5}$$

where $\hat{\mathbf{R}} = \frac{\mathbf{R}}{|\mathbf{R}|}$ and $\mathbf{R} = (-v_F k_y, v_F k_x, m)$, 2 prefactor is because we have top and bottom

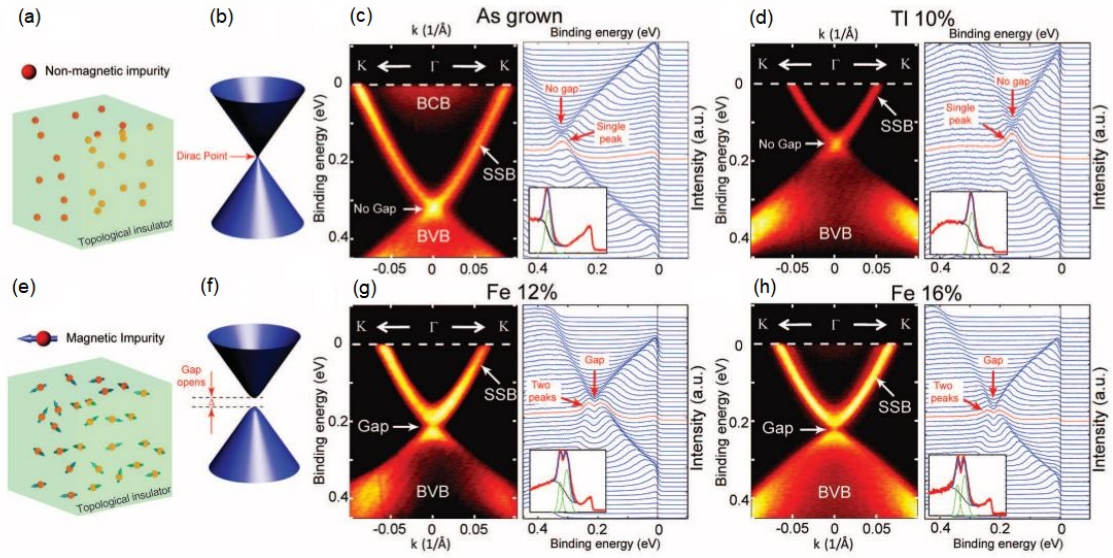

Figure 2.6: (a) and (b) A nonmagnetically doped topological insulator with a Dirac point connecting the upper and lower Dirac cones as in the undoped case. (c) Band structure along the $K-\Gamma-K$ direction of undoped Bi_2Se_3.Left and right subpanels show the ARPES spectral intensity plot and a stacking plot of the energy distribution curves (EDCs), respectively. The red curve in the right subpanel indicates the EDC at the Γ point. Inset: EDC at the Γ point (red), fitted with a Lorentzian peak (green) on the Shirley background (black); the total fitting function is shown in blue. The same convention is used in (d),(g), and (h). (d) Band structure for a Tl-doped sample, $(Bi_{0.9}Tl_{0.1})_2Se_3$. The Dirac point remains continuous. (e) and (f) A magnetically doped topological insulator with a broken Dirac point and a gap separating the upper and lower Dirac cones. (g) and (h) Band structure of two Fe-doped samples from two growth batches with melt composition $(Bi_{0.88}Fe_{0.12})_2Se_{3.7}$ and $(Bi_{0.84}Fe_{0.16})_2Se_{3.7}$, respectively. At the Dirac point, the reduced spectral intensity (left subpanels) and the twin-peak structure in the EDCs (right subpanels) indicate a gap formation. Figure is adopted from [5].

surfaces.

As one can see from equation 2.5, Chern number is just +1 or -1, depending on the sign of m parameter in the Hamiltonian 2.4. Physically the sign of m depends on the projection of magnetization on the normal to the surface of crystal $sgn(m) = \mathbf{M} \cdot \mathbf{n}$, where $\mathbf{M}$ is a magnetization and $\mathbf{n}$ is normal vector to the surface.

All topological invariants are measurable quantities. In the case of Chern insulators one of the measurable features is quantum anomalous Hall effect (QAHE)[4]. That is why such a material is also called a quantum anomalous Hall insulator (QAHI). The point of this effect is that we have quantized Hall conductivity at zero magnetic field:

$$\sigma_{xy} = \frac{e^2}{h} \cdot C = \pm \frac{e^2}{h}, \tag{2.6}$$

where h is a Planck‘s constant, e is charge of an electron.

For the first time, QAHE was measured in epitaxial thin films of $(Bi,Sb)_2Te_3$ doped with chromium at a temperature of 30 mK [6]. Fig.2.7(a) shows dependence of Hall resistivity

on external magnetic field and at different gate voltages. Gate voltage is necessary, because to observe QAHE it is necessary to put Fermy energy to the magnetic gap to suppress transport on the surface and allow transport only through 1D chiral end state. As it's seen from this data, QAHE is observes only in the narrow region of gate voltage and at mK temperature range.

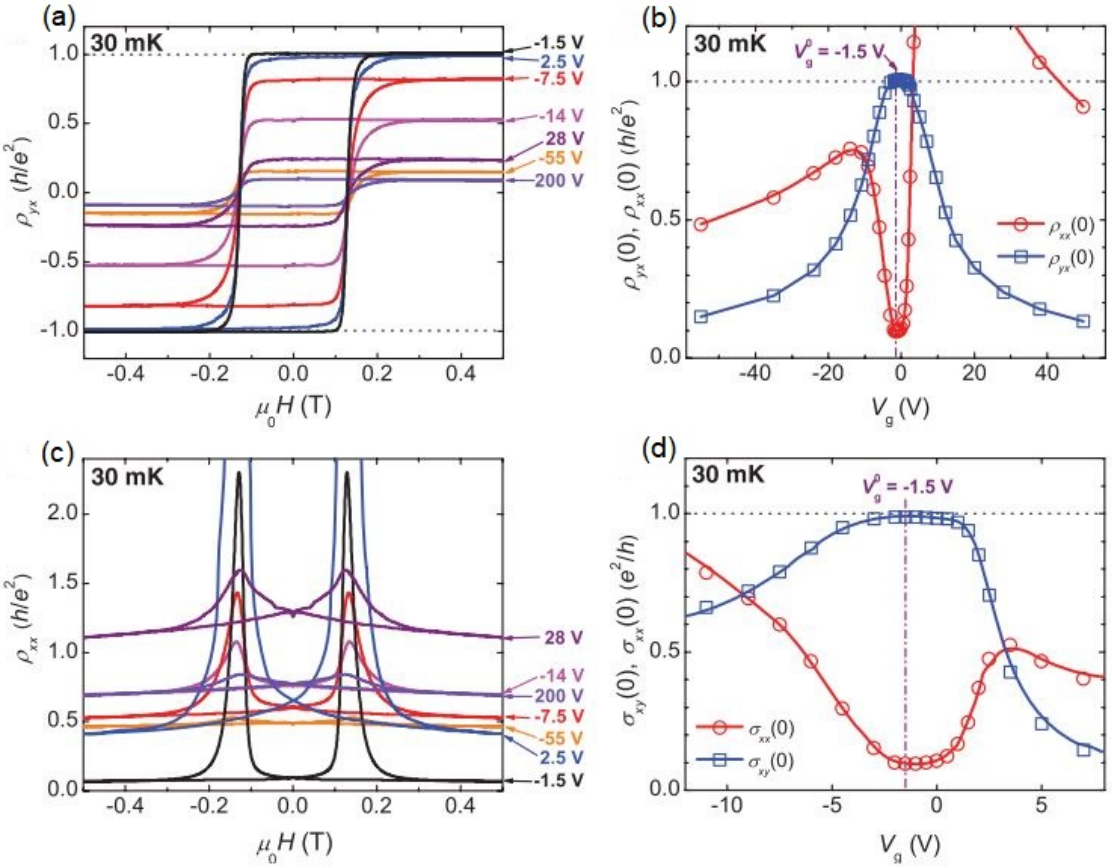

Figure 2.7: (a) Magnetic field dependence of ρ_{xy} at different V_g. (b) Dependence of $\rho_{xy}(0)$ (empty blue squares) and $\rho_{xx}(0)$ (empty red circles) on V_g.(c) Magnetic field dependence of ρ_{xx} at different V_g. (d) Dependence of $\sigma_{xy}(0)$ (empty blue squares) and $\sigma_{xx}(0)$ (empty red circles) on V_g. Figure is adopted from [6].

However, taking into account the size of the magnetic gap (on the order of tens of meV), the quantum anomalous Hall effect should be observed at higher temperatures (the Curie temperature in these films is usually several tens of Kelvin). As it is shown in [7], one of the reasons that ultra-low temperatures are needed is the proximity of the chemical potential to the valence band. On the one hand, the Fermi level should be located in the magnetic gap, but on the other hand, the magnetic gap is located too close to the valence band. Therefore, as the temperature rises, transport through trivial bulk channels begins to dominate, and the exact quantization of the Hall conductivity ceases to be observed. In [8] Arakane and collaborators show that by varying the composition in the four-component material $Bi_{2-x}Sb_xTe_{3-y}Se_y$, it is possible to raise the Dirac point upward in energy, thereby increasing the distance to the valence band. If we introduce ferromagnetic order in such a

material and ensure that the Fermi level is located in the magnetic gap, then there is hope that it will be possible to realize the quantum anomalous Hall effect at higher temperatures. It was shown [9], that it is possible to grow bulk crystals of a four-component topological insulator $Bi_{2-x}Sb_xTe_{3-y}Se_y$ (see Fig.2.8(a)) and induce ferromagnetism by doping the samples with Fe.

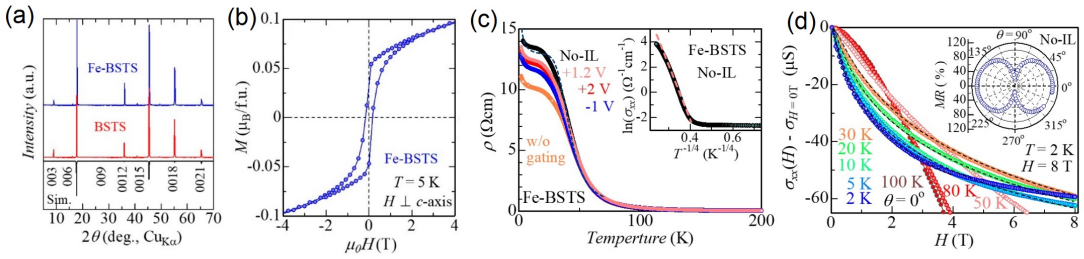

Figure 2.8: (a) XRD pattern for BSTS and Fe-BSTS. (b) Magnetization hysteresis loop for Fe-BSTS taken at 5K. (c) Temperature dependence of bulk Fe-BSTS crystal. (d) Magnetoresistance as a function of top-gate voltage and angle. Figure is adopted from [9] and [10]

A magnetization hysteresis loop was demonstrated at 5 K, suggesting ferromagnetism in this material. The R(T) dependence indicates that at temperatures below 50 K, surface transport predominates even in bulk crystals. At low temperature there is an upturn of resistivity, likely due to the magnetic gap opening. So, this material is an excellent candidate for observing QAHE on it at higher temperatures.

2.3 Topological superconductors

Closely related to topological insulators is the concept of Majorana fermions. It is a fermion that is its own antiparticle $\gamma = \gamma^\dagger$, where γ is an annihilation operator for this particle. The existence of such particles was predicted a very long time ago in high-energy physics [11], but to this day their existence as elementary particles remains in question.

Generally speaking, every fermionic operator f can be written in terms of two Majorana operators γ_1 and γ_2:

$$f = (\gamma_1 + i\gamma_2)/2 \tag{2.7}$$

$$f^\dagger = (\gamma_1 - i\gamma_2)/2 \tag{2.8}$$

But recently, it was theoretically demonstrated (see, for example, [12]) that Majorana particles can be formed in a topological superconductor at topological defects (vortices or sample boundaries). The main feature is that two Majorana fermions in topological superconductor γ_1 and γ_2 are separated in space. This allows us to study all the beautiful physics related to Majoranas just "on the table".

Superconductivity

Cooling down some conductors bellow a certain temperature (critical temperature T_c), turns them into superconducting phase. This phase is characterized by zero resistance and so called Meissner effect (magnetic field can not penetrate to the bulk of superconductor).

The origin of this phenomena is the electron–phonon interaction, due to which two electrons with opposite spins interact with each other and form Cooper pairs. Pair of fermions (electrons) is boson, therefore Bose–Einstein condensation can occur. Therefore, all electrons in a superconductor at T=0 are coherent and described by a single wave function (order parameter of the system):

$$\Psi = |\Psi| e^{i\theta}, \tag{2.9}$$

where $|\Psi|$ is its amplitude, and θ is the phase. The characteristic distance between two electrons in Cooper pair is called the coherence length:

$$\xi_s = \hbar v_F / \pi \Delta, \tag{2.10}$$

where v_F is the Fermi velocity, Δ is the energy gap in the spectrum of the superconductor. The coherence length ranges from one to several hundred nanometers, depending on the material.

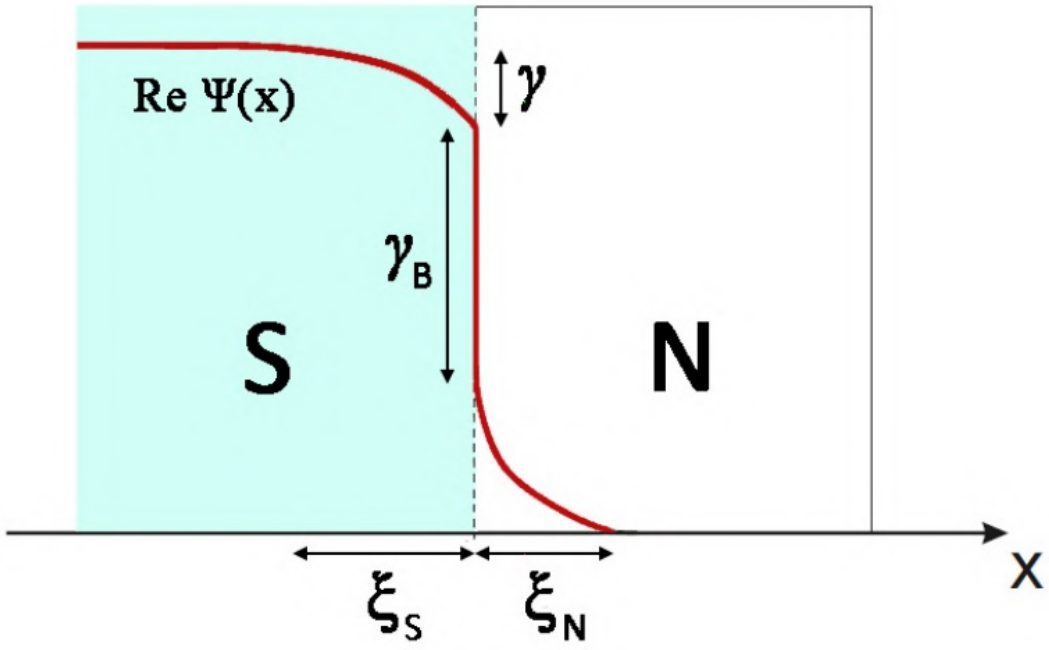

Figure 2.9: Schematic representation of real part of order parameter as a function of coordinate at the SN boundary. S represent superconducting region, and N is a normal metal. ξ_s and ξ_N are coherent length in the superconductor and the normal metal, respectively. γ_B is a transparency of the interface.

In the case of a homogeneous superconductor, all characteristic quantities in it have

constant values. In hybrid superconducting samples Δ becomes a spatially dependent quantity, which leads to the emergence of new effects, for example, proximity effect.

Let's consider a boundary between superconductor and normal metal (see Fig.2.9).

In this case, normal metal close to the superconductor become superconducting, but superconductor near normal metal become less superconducting (the absolute value of the order parameter is less than far away from the boundary). Superconducting correlations between electrons in the diffuse normal metal can be observed at a distance of the order of the coherence length of the metal ξ_N. They exponentially (e^{-x/ξ_N}) decay into the normal metal near the SN interface.

A decrease in the density of Cooper pairs in a superconductor near the SN interface is determined by the parameter $\gamma = \rho_S\xi_S/\rho_N\xi_N$ (ρ_S and ρ_N are the resistivities of S and N metals in the normal state). Transparency parameter $\gamma_B = R_B/\rho_N\xi_N$ (R_B is the resistance of the SN interface unit area) defines the jump of Ψ on the SN interface (Fig.2.9).

If we consider two SN boundaries, rather than one, such structure is called SNS Josephson junction, and the feature of this device is that if the distance between two superconductors is not large, the supercurrent can flow through this system, e.g. we have coherent transport of Cooper pairs through the N region.

S/MTI heterostructures

Today there is no strong evidence that topological superconductors exist as material, but it can be obtained due to the proximity effect in topological insulator/superconductor heterostructures [13]. The interest in such materials is due to the fact that Majorana bound states should have non-Abelian statistics, therefore they can be used to create qubits, and then - topological quantum computers that are resistant to local sources of decoherence, as, for example, presented in the work with an array of one-dimensional nanowires [14]. However, to date, there is no unambiguous experimental confirmation of the existence of Majorana modes and their non-Abelian statistics.

Another way to create a topological qubit is to use chiral Majorana fermions [16], which should be formed in chiral topological superconductors (CTS). It was shown that such a superconductor can be obtained by inducing superconductivity in QAHI due to the proximity effect [17], that is, in superconductor/magnetic topological insulator heterostructures. Let us start from the Hamiltonian of Chern insulator (2.4), but include hybridization between the top and bottom surface states $m(k) = m_0 + m_1(k_x^2 + k_y^2)$:

$$H_0(\mathbf{k}) = k_y\sigma_x\tau_z - k_x\sigma_y\tau_z + m(k)\tau_x + \lambda\sigma_z, \tag{2.11}$$

where $\tau_i (i = x, y, z)$ are Pauli matrices in space of top/bottom surfaces. In proximity to an s-wave SC, a finite pairing amplitude is induced in the QAH system. The Bogoliubov-de

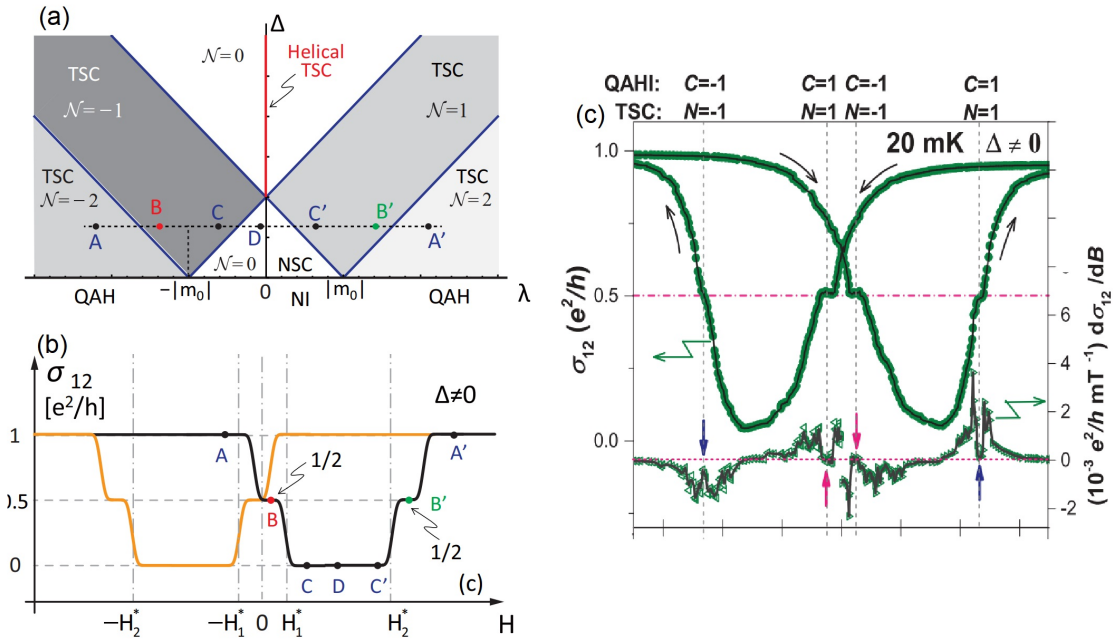

Figure 2.10: (a) Phase diagram of the QAHI-SC hybrid system. (b) Dependence of two-terminal resistance of QAHI-SC hybrid structure as a function of external magnetic field. Different plato correspond to different topological phases. (c) The same dependence, measured in experiment [15].

Gennes (BdG) Hamiltonian becomes:

$$H_{BdG} = \begin{pmatrix} H_0(\mathbf{k}) - \mu & \Delta_{\mathbf{k}} \\ \Delta_{\mathbf{k}}^{\dagger} & -H_0^*(\mathbf{k}) + \mu \end{pmatrix}, \tag{2.12}$$

where μ is chemical potential, $\Delta_{\mathbf{k}}$ is the pairing potential:

$$\Delta_{\mathbf{k}} = \begin{pmatrix} i\Delta_1\sigma_y & 0 \\ 0 & i\Delta_2\sigma_y \end{pmatrix}, \tag{2.13}$$

where Δ_1 and Δ_2 are pairing gap functions on top and bottom surface states, respectively.

It can be shown that this Hamiltonian is equivalent to the $p_x + ip_y$ topological superconductor. Depending on the parameters, there are few topological phases could exist, as shown in Fig.2.10(a). N is a topological invariant, which is related to the number of Majorana modes at the boundary. We are mostly interested in the $N = 1$ phase, because it means that we have single chiral Majorana mode at the boundary of topological superconductor, and 2 chiral Majorana modes are just equivalent to single fermionic mode, so $N = 2$ topological superconductor is equivalent to $C = 1$ QAHI.

Chiral Majorana modes in such systems should lead to the fact that the conductivity of the QAHI/CTS/QAHI heterostructures should be half the quantum of resistance (Fig.2.10(b)). The conductance is exactly half because there is 50% probability that electron

going through chiral channel will be reflected back to the another edge. Similar behavior was observed in the experiment [15], which is presented in Fig.2.10(c). Indeed, they observed 0.5 conductance plato, however, there is an alternative explanation for this effect that does not involve chiral Majorana modes [18]: superconductor may play a role of metal short cut, electricaly connecting left and right chiral chanel in QAHI, resulting in the same half-quantization.

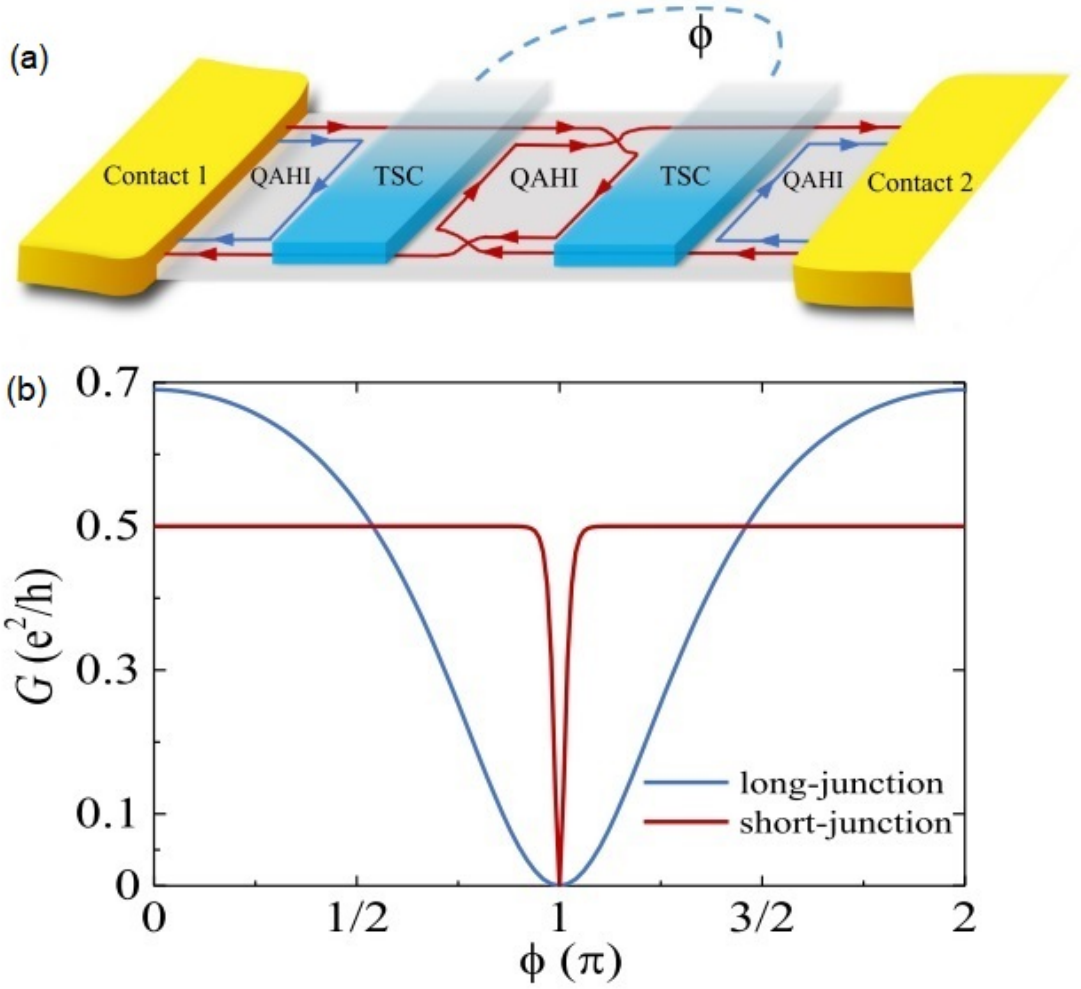

Figure 2.11: (a) Schematic representation of a Majorana-Josephson interferometer. A quantum anomalous Hall insulator (gray) is in contact with two superconductors (blue) and two normal leads (yellow) at its ends. The arrowes represent trajectories of chiral Majorana modes in the interferometer. (b) Two-terminal conductance G as a function of phase difference in a Majorana-Josephson interferometer when the Josephson junction is long (blue curve) and short (red curve), respectively. Figure is adopted from [19].

Thus, to date, there is also no reliable evidence in favor of the existence of chiral Majorana fermions. It can be obtained, for example, by performing the experiment proposed in [16]. Lian and collaborators proposed Majorana interferometer, which can show coherent oscillations of the conductance vs gate voltage, proving existence of chiral Majorana fermions in that sistem. Or in the work of Li and collaborators [19], it was proposed the model of Majorana-Josephson interferometer, where the conductance of device (Fig.2.11(a))

is controlled by the phase difference between two superconductors (Fig.2.11(b)). In both cases the central element of the topological qubit is the proximity induced superconductivity to the magnetic topological insulator.

Chapter 3
Technological and Experimental Methods

The fabrication and research of hybrid superconducting systems based on magnetic topological insulators requires a multi-stage approach using a variety of high-tech equipment. This chapter is devoted to the description of the entire technological cycle of work: from the fabrication of hybrid superconducting structures based on magnetic topological insulators to the methods of studying the electron properties of such structures.

3.1 Scanning Tunneling Microscopy

In order to characterize the properties of electrons in crystals, a variety of techniques can be used, depending on the information we want to obtain about the material under study. If we are interested in the surface properties of electrons, Scanning Tunneling Microscope (STM) can provide a lot of information about the surface of the material. In this work, we are interested in topography and spectrum of electrons (e.g. density of states as a function of energy).

Applying the voltage difference between the surface of the sample and the metallic tip, which is brought to a distance of several angstroms to the surface, electrons will tunnel from the tip to the surface or backward. This is the fundamental principle of STM. This phenomenon is based on a purely quantum effect. In the classical case, electrons do not have enough energy to cover the distance between the tip and the sample surface. However, in the case of quantum mechanical tunneling electrons can overcome the spacing with a certain non-zero probability. The current which flows from the sample surface to the tip or conversely is produced by the tunneling electrons. Diverse characteristics affect the tunneling current value. For example, the tunneling current depends on the distance between the surface and the tip exponentially: the closer the tip to the surface is, the higher the current is; and vice versa, the farther the tip is, the less the current is. The controlling of the height is performed by using the piezoelectric element of the scanner (usually, the tube), which expands if a voltage is applied to it.

One of the opportunities of the STM is obtaining a topographic image. For maintaining the tunneling current to be constant, the distance between the sample surface and the tip should be fixed. That is possible due to managing the height of the metallic tip by changing the voltage applied to the piezoelectric tube. Moving parallel to the sample surface

the tip scans the surface plane remaining at a constant height above it (the tunneling current is retained constant too). Even in the case, the sample surface is not absolutely flat, the tip will repeat topography on the fixed height above it (see Fig.3.1(a)). So, to keep the set-point current, the applied to the piezoelectric tube voltage can be computed to the height of the tip. Thereby we obtain the height map of the sample surface [20].

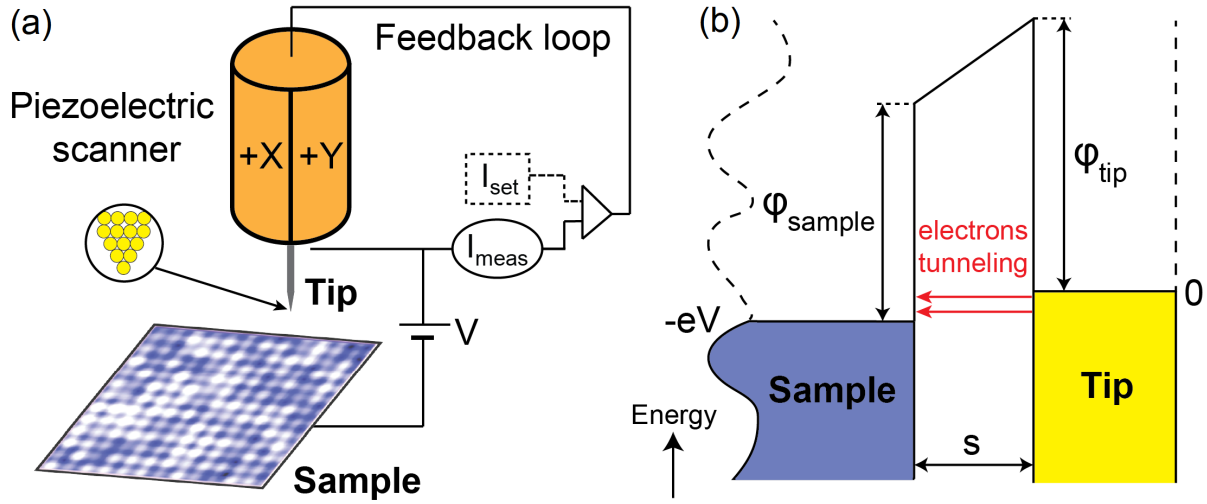

Figure 3.1: (a) The scheme of the constant current imaging. The typical distance between the tip and the surface d is about $5-10$ $\mathring{A}$. The tip has an unrealistically sharp shape in the picture. (b) The tunneling in the energy space. The ϕ_{sample} and ϕ_{tip} are the work functions of the sample surface and the tip, respectively. The electrons from the tip can tunnel to the sample surface.

To understand the physics behind this technique, let us consider the equation of the tunneling current (from the sample surface to the tip) [21]:

$$I = \frac{2\pi e}{\hbar} \int_{-\infty}^{\infty} |M_{\mu\nu}|^2 g_{Sample}(E) g_{tip}(E + eV_{Bias}) n_{FD}(E)[1 - n_{FD}(E + eV_{Bias})]dE, \qquad (3.1)$$

where $g_{Sample}(E)$ and $g_{tip}(E)$ are the local density of states (LDOS) of the sample surface and the tip, n_{FD} is a Fermi-Dirac distribution, $M_{\mu\nu}$ is a matrix element transition from the sample surface (from ψ_μ state) to the tip (to ψ_ν state). It can be interpreted as follows: the tunneling can be provided by only electrons from the **filled state** in the sample ($g_{Sample}(E)n_{FD}(E)$) to the **empty state** in the tip of the same energy, considering the energy shift provoked by the bias voltage ($g_{tip}(E+eV_{Bias})[1-n_{FD}(E+eV_{Bias})]$) (see Fig.3.1(b)). This expression can be derived using the Fermi's golden rule.

Let us make some simplifications:

1) $g_{tip} \neq g_{tip}(E)$, e.g. DOS of metal tip is approximately constant near the Fermi energy E_F in the range of small bias voltages. So, g_{tip} goes out of the integral.

2) n_{FD} is a step function, e.g. the zero temperature limit. At finite temperature, it

is still a good approximation if $k_BT << E_F$. So, the Fermi-Dirac distribution turns into a change of integration limits.

3) Essentially, the matrix element $M_{\mu\nu}$ is the probability current from the sample to the tip. Thus, if we assume that a tip is a sphere and the wavefunction of the surface is the same as for planar surface, the $M_{\mu\nu}$ will be presented as:

$$M_{\mu\nu} \propto |\psi_\mu(\overrightarrow{r_0})|^2 \propto e^{-2\kappa d}, \tag{3.2}$$

where $\overrightarrow{r_0}$ is a vector from the point under the tip to the center of the sphere (the end of the tip), $\kappa = \frac{(2m\phi)^{\frac{1}{2}}}{\hbar}$, ϕ is the difference between the Fermi energy of the sample and the energy of the free-electron state of the vacuum, d is the distance between the sample surface and the tip.

Finally, taking into account above assumptions the tunneling current takes the form:

$$I \propto e^{-2\kappa d} \int_{E_F}^{E_F+eV_{Bias}} g_{Sample}(E)dE. \tag{3.3}$$

The fact that the tunneling current depends on the distance between the tip and the sample exponentially leads to the STM is a very precise technique for imaging the topography of the surface.

The most intriguing consequence for fundamental physics is that the tunneling current is an energy integral of DOS. It can be written in the following form:

$$\frac{dI}{dV_{Bias}} \propto g_{Sample}(E + eV_{Bias}). \tag{3.4}$$

In this way, if the tip is keeping its position above the sample surface during the time of varying the bias voltage, we will obtain the local density of states near the Fermi level. We can investigate the occupied and the unoccupied local DOS of the sample because we can apply positive and negative voltages.

So, varying the bias voltage in the interesting range in the certain position (x, y) above the surface gives a spectrum $g(E)$ at this point. The zero bias voltage corresponds to the Fermi energy E_F of the sample. To obtain the 3D dataset $g(E, x, y)$ (where x and y are spatial dimensions, E is energy dimension), we need to represent the surface as a grid and to measure the spectrum of each point of this grid in the plane are x and y coordinates, the color is the value of dI/dV_{Bias}.

The principal scheme of the STM is shown in Fig.3.2. The current value is detected for different applied voltages, and the current-voltage curves are recorded for each point of the grid to the file on the computer. The "distance control and scanning unit" is a module for tip displacement and controlling the distance between the tip and the sample.

In this work, we used a unique version of a scanning probe microscope based on the Joule-Thomson effect, intended for measuring the topography of conducting surfaces and

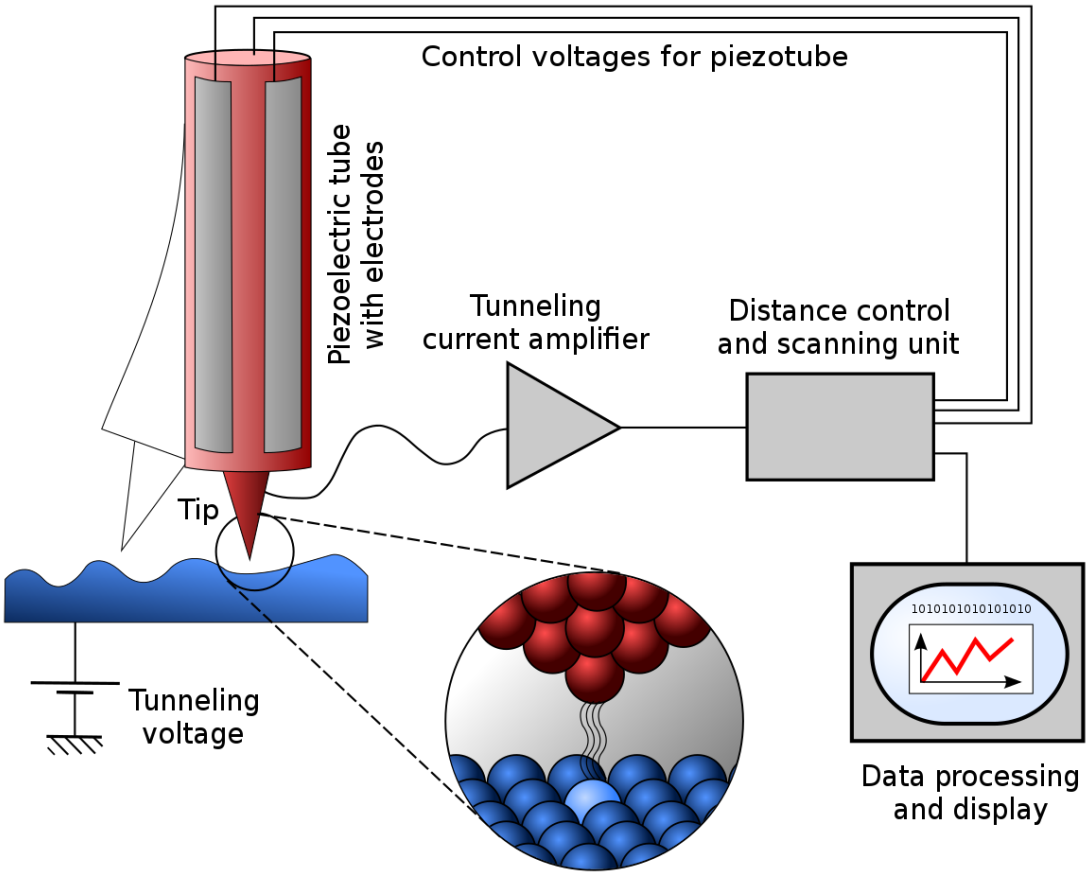

Figure 3.2: The principal scheme of the Scanning tunneling microscope.

spectroscopy with high spatial resolution. This microscope belongs to the equipment in the field of ultra-high vacuum technologies. Photo of the microscope is presented in Fig.3.3.

The holder with a sample or with a tip is loaded from the atmosphere inside the Load Lock. Firstly, it is evacuated by the spiral pump, and later, when the pressure will reach the value $\sim 0.1\ mbar$, the turbomolecular pump is turned on. At $10^{-7}\ mbar$ the holder is moved to the Preparation Chamber, where the pressure can reach $10^{-10}\ mbar$ by the turbomolecular and the sublimation pumps. From the Preparation Chamber, the holder with a tip can be moved to the Ion Etching Chamber. Finally, the sample can be moved from the Preparation Chamber to the STM Chamber, where measurements are carried out. The pressure of the STM Chamber is supported by the ion pump at a level $10^{-10}\ mbar$. So, during the experiment only ion and sublimation pumps are working, while the spiral and the turbomolecular pumps are turned off, which allows avoiding noises created by mechanical vibrations.

Four slots are used for storing reserve tips or samples in the STM Chamber. Measurements are conducted inside three thermo-insulating shields to avoid heating of the system for low-temperature experiments. Pneumatic supports of the STM chamber are used to reduce vibrations.

JT-STM can provide the temperature about $\sim 1\ K$. It is possible because the liquid

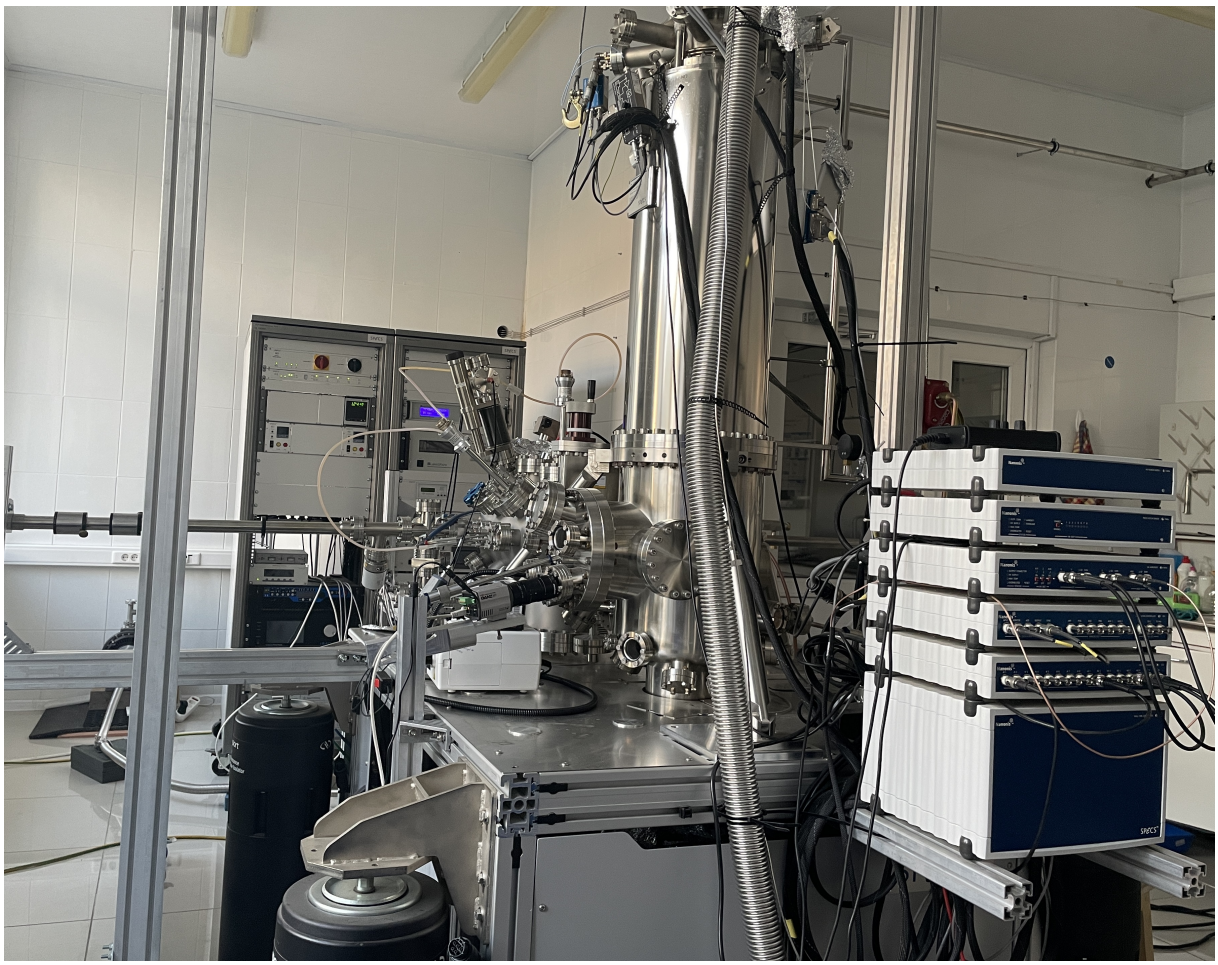

Figure 3.3: Photo of the scanning tunneling microscope, placed in Laboratory of Topological Quantum Phenomena in Superconducting Systems, MIPT.

helium inside the inner reservoir supports the $T = 4.2\ K$ and due to Joule–Thomson effect the $1\ K$ is achieved. The helium reservoir is surrounded by nitrogen ($T = 77\ K$) for preventing the rapid evaporation of helium. It is possible to work at $T = 77\ K$, when the nitrogen is inside both reservoirs. The electromagnet, which is located near the microscope, lets to apply the transverse magnetic field up to $3\ T$. STM measurements are conducted by using the Nanonis electronics and software. For our measurements, we used hand-made tungsten tips. The whole procedure of tip fabrication can be found in [22].

3.2 Angle-resolved photoemission spectroscopy

Angle-resolved photoemission spectroscopy (ARPES) is used to determine the band structure of solids. In this work we used synchrotron radiation to excite the solid since it allows us to tune the energy of photons in a wide range. Also, synchrotron radiation is characterized by high intensity, small uncertainty in energy, and it can be focused on a small beam to collect photoelectrons from a spot of tens of micrometers. Synchrotron radiation is generated in the following way. The magnetic field deflects the electrons, which have large

energy, and when these electrons change direction (going in circles) they emit radiation. This radiation is going into the beamline, where it is monochromatized by a diffraction grating and focused on the surface of the sample under study. We used linear horizontal polarization beam with energy $h\nu = 15$ eV.

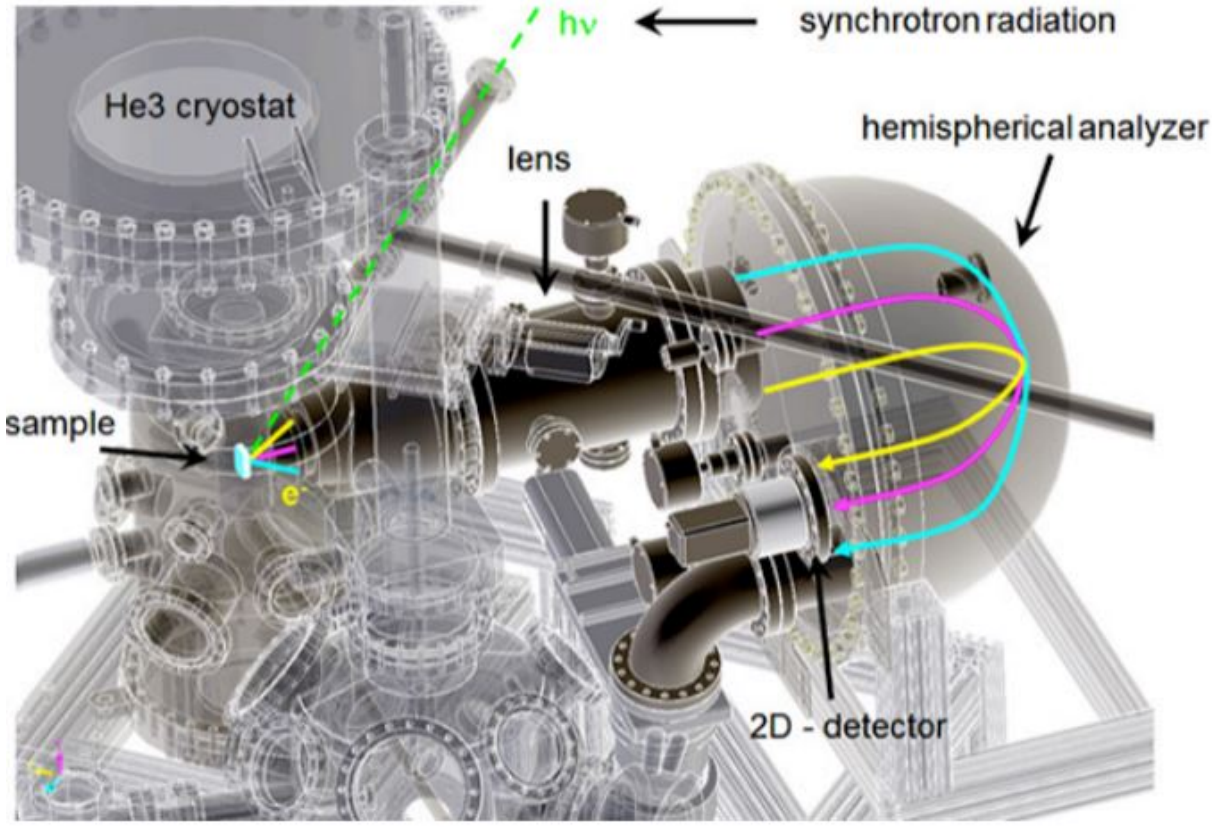

Figure 3.4: Schematic of the ARPES setup. Yellow, purple and blue traces correspond to different tilt angles. Green dashed line correspond to the incoming x-ray beam. Figure is adopted from [23]

The main part of ARPES set-up is the analyzer of electron energy (Fig.3.4). Since we are interested in the kinetic energy of the outgoing electrons and the angle of outgoing electrons, it would be convenient to detect both characteristics in a single measurement. To do so, there is a simple principle. The electron-optical lens focus electrons which left the surface at some angle to a point in the focal plane (Fig.3.4). In such a way we get information about the momentum space. The distance from the focal plane to the electron peak corresponds to the angle, at which electrons leave the surface, and therefore to the momentum of the electrons. To analyze the energy of electrons, the entrance slit of the hemispherical analyzer is placed precisely in the focal plane of the electron-optical lens. Voltages on two hemispheres are chosen in such a way that only electrons with known kinetic energy will be going exactly in the middle of two hemispheres and focused on the center of the detector. Faster electrons will hit the detector closer to the outer hemisphere; slower electrons will hit the inner hemisphere. That is how we can get the photoemission intensity as a function of the momentum of electrons and the energy of electrons simultaneously.

There are few reasons to conduct the measurements at low temperatures. Firstly, if the temperature of the material is high, the electronic states are blurry in energy and momentum. To measure the band structure with high precision this temperature broadening has to be as small as possible. Secondly, a lot of physical properties are temperature-dependent (superconductor transitions, magnetic transitions, and so on), and to know the properties of those systems as a function of energy is of fundamental importance. One of the effective ways to cool the sample down to tenths of a Kelvin is to use liquid helium. Typically, reaching sub-Kelvin temperatures is not hard, because thermal radiation can be effectively shielded. Unfortunately, we can not do the same in photoemission experiments because we need to light the sample by x-rays and collect outgoing electrons. This is realized by specially designed slits in radiation shields, which have different temperatures. The cooling power of the cryostat should be very high to compensate for the heat coming from the x-ray beam and room-temperature environment. This is achieved by using two pumps which reduce the vapor pressure above the liquid He3, therefore cooling the sample. The sketch of the photoemission experiment is shown in Fig.3.4. The x-ray beam goes to the 1 K surface of the sample and knocks photoelectrons out. Electrons are projected to the entrance slit of the analyzer, sorted in terms of momentum, and then the kinetic energy is measured.

3.3 Mechanical exfoliation

The first stage in the preparation of structures is fabrication of thin flakes of crystals by mechanical exfoliation. The so-called scotch tape technique was firstly utilized to obtain graphene from graphite in 2004. After that, a lot of thin films of other materials, such as $h-BN$, MoS_2, Bi_2Se_3, and others were obtained by mechanical exfoliation. This method of producing thin flakes is possible because the above materials are so-called van der Waals crystals. They are layered materials, in which the bonding between different layers is weak van der Waals force. It makes possible easy mechanical cleavage along some crystallographic planes.

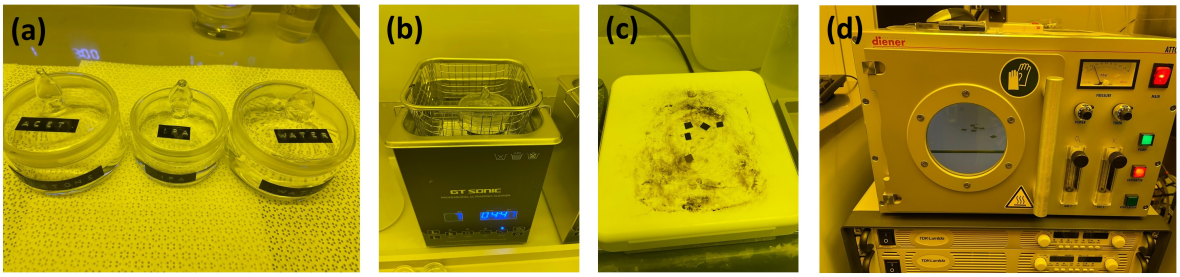

Figure 3.5: The procedure of substrate cleaning. (a) The sequence of solvents: Acetone, IPA, DI Water. (b) Substrates in an ultrasonic bath. (c) Substrates on a hot plate. (d) Substrates inside Ar-plasma etching machine.

First, Si/SiO_2 substrates were cleaned to remove organic contaminants and water

from the surface (see Fig.3.5). The following procedure was used:

1) Ultrasonic cleaning in Acetone for 5 minutes,

2) Ultrasonic cleaning in 2-propanol (IPA) for 3 minutes,

3) Ultrasonic cleaning in deionized water (DI) for 1 minute,

4) Annealing at 120 degrees C for 5 minutes on a conventional laboratory hot plate,

5) Oxygen plasma cleaning for 5 minutes.

Second, bulk single crystals of magnetic topological insulators were placed on the adhesive side of blue tape and slightly pressed in a few places. Then transferred crystals were thinned by multiple pilling-off procedures. Third, the crystals-loaded tape was brought in contact with the substrate, slightly pressed by a finger, and relatively slowly released. The example of exfoliated flakes can be seen in Fig.3.6(d).

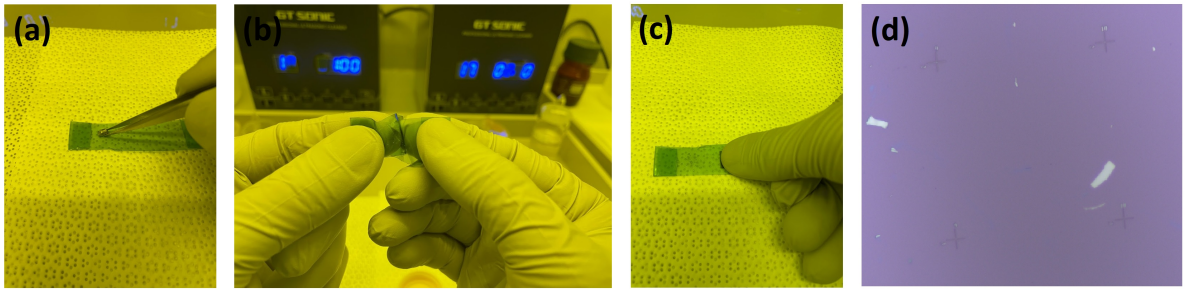

Figure 3.6: Exfoliation procedure. (a) A single crystal is placed on scotch tape. (b) Multiple pilling off. (c) Flake transfer to the substrate. (d) Examples of exfoliated flakes.

3.4 Atomic force microscopy

In order to determine the topography and height of exfoliated flakes under study, we used an atomic-force microscope from NanoScan Technology. It allows us to determine the position of the cantilever with respect to the substrate using an integrated optical microscope, so, we can easily scan the flake we are interested in.

The principle of the work of the atomic force microscope is based on the detecting force interaction between a sample surface and a tip. The nanoscale tip is used as a probe and locates on the end of the elastic console, which is called a cantilever. The force acting on the probe from the surface side causes the console to bend. The appearance of hills or pits under the tip leads to a change in the force acting on the probe, and therefore to a change in the bending value of the cantilever. Thus, by detecting the bending value, we can get an image of the surface topography (see Fig.3.7(b)). Forces acting between the probe and the sample are short-range van der Waals forces (see Fig.3.7(c)). These forces may be positive or negative: at long distances, they provide attraction, at short distances they provide repulsion.

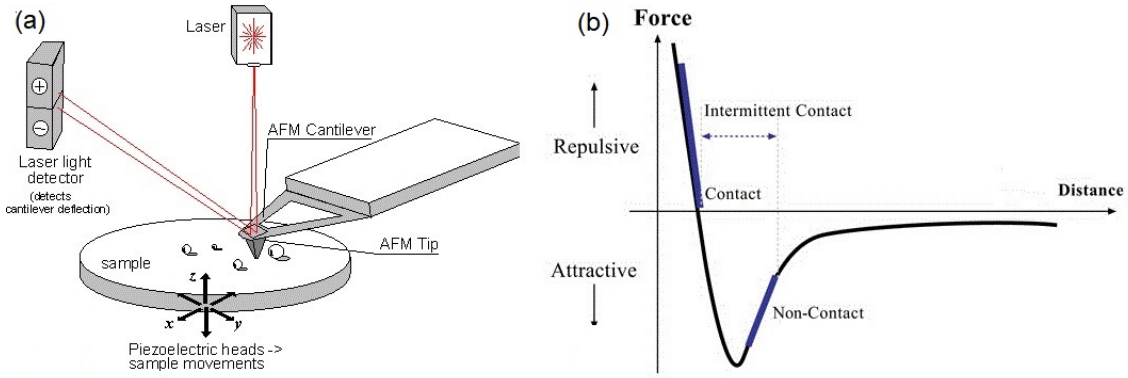

Figure 3.7: Schematic representation (a) and regimes (b) of the work of the atomic force microscope.

NST microscope operates in semi-contact mode. During the measurements in the semi-contact mode vibrations at the resonant frequency are excited on the cantilever. The force acting from the surface side leads to the shift of amplitude-frequency and phase-frequency characteristics of the tip, thus the amplitude and the phase change their values, meanwhile, feedback maintains the amplitude to be fixed. The change of the amplitude and the phase are detected, which allows obtaining the desired image. Fig.3.8 shows the topography of the Fe-BSTS flake and corresponding height profiles.

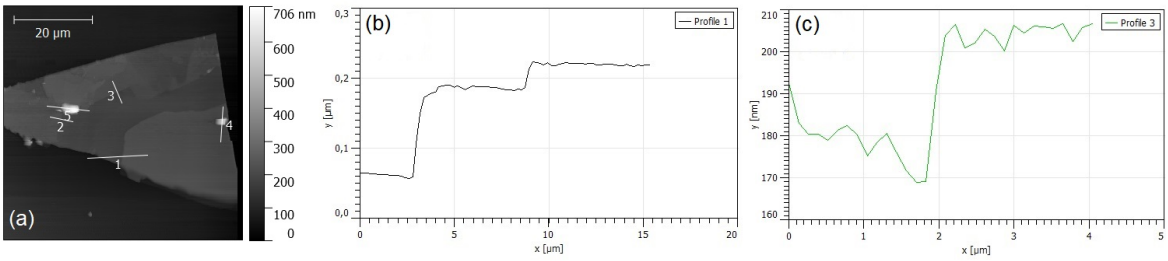

Figure 3.8: (a) Topography of the exfoliated crystal. (b) and (c) Height profile along lines 1 and 3, respectively.

3.5 Lithography

In order to develop the design of a structure with a magnetic topological insulator flake, it was necessary to bind the required object to coordinates. The coordinates of the flake selected on the substrate were determined using an optical microscope via coordinate crosses (see Fig.3.9(a)). After selecting the best specimens, a drawing of contact leads to flake was made in the AutoCAD environment. Screen Shot of the design of SQUID is shown in Fig.3.9(b). The resulting drawing was converted in a format compatible with the software of the electronic lithograph Crestec Cable 9000, located at the MIPT Center for Collective Use.

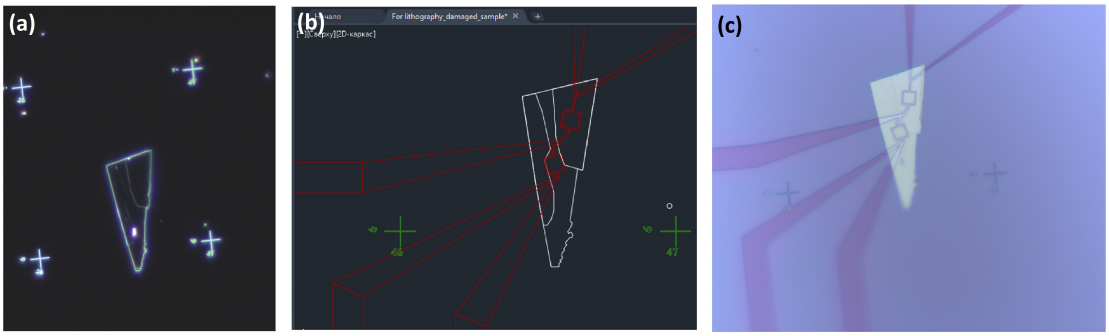

Figure 3.9: Example of the lithography process. (a) Dark-field optical image of exfoliated flake near coordinate crosses. (b) Design of sample in AutoCAD. (b) Optical Image of the developed resist.

Then the substrate was covered by two layers of PMMA A4 resist using spincoater (6000 rpm, 30 s). Baking of each layer was conducted in a furnace at 50° C for 4 hours in order to prevent the degradation of the sample surface during heating. The desired structure was formed by an electron beam, the dose was 450 $\mu C/cm^2$ at electron beam currents of 150 pA for thin structures and 4000 pA for contact pads. The development of the structure was carried out in a preliminary prepared solution of methyl isobutyl ketone and isopropyl alcohol (1:4) for 90 sec. Photo of the developed resist is shown in Fig.3.9(c).

3.6 Magnetron sputtering

The next step was the metallization of an electronic resist mask (exposed contacts connected to flakes) by a superconductor in an ultra-high vacuum magnetron setup (Fig.3.10).

Niobium was chosen as a superconductor because it forms a transparent interface with topological insulators. The preliminary vacuum in the deposition chamber was $p_0 = 2 \times 10^{-9}$ mbar. It is important to note that, before the deposition of the superconductor, the substrate with flakes was etched in argon plasma to clean the surface of topological insulators from oxide and organic contamination. Treatment parameters: P=80 W (reflected power $P_{refl} = 0$ W), PowerStep = 10 W, $V_{DC} = 234$ V, $p_{Ar} = 2.15 \times 10^{-2}$ mbar, etching of 15 seconds was conducted. During this time, approximately 5 nm of the surface layer is etched away, which was determined using AFM.

After etching the sample, superconducting niobium was deposited. The thickness of the deposited metal was chosen based on the thickness of the flakes. Spraying parameters: $p_0 = 8.6 \times 10^{-9}$ mbar, P=200 W, $V_{DC} = 238$ V, $p_{Ar} = 4 \times 10^{-3}$ mbar, deposition rate V=0.1 nm/s. It should be noted, that since the magnetron targets are located at an angle to the stage where the sample is located, for better lift-off, we used a tilted table (see Fig.3.11(a)). The final step in planar superconducting device fabrication is lift-off, which was made in acetone.

The final device is shown in Fig.3.11(b). As one may see, there is some problem with

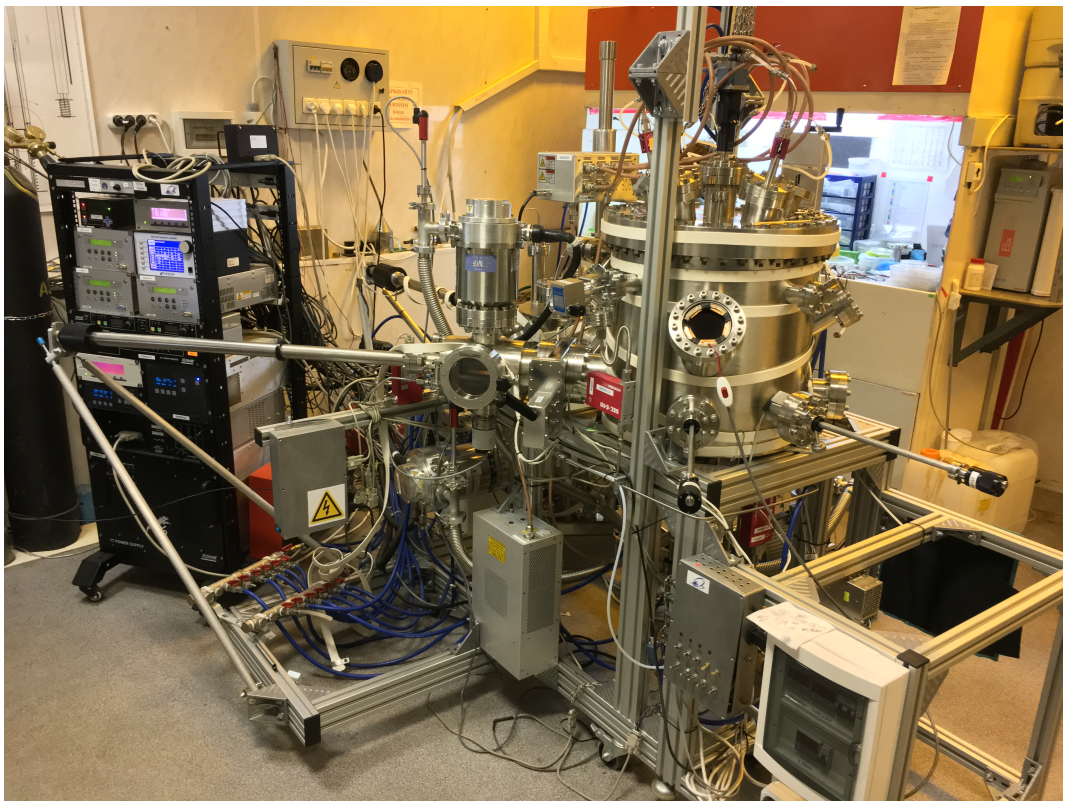

Figure 3.10: Ultra-high vacuum complex for magnetron sputtering and electron-beam evaporation. Designed and assembled by V.S. Stolyarov.

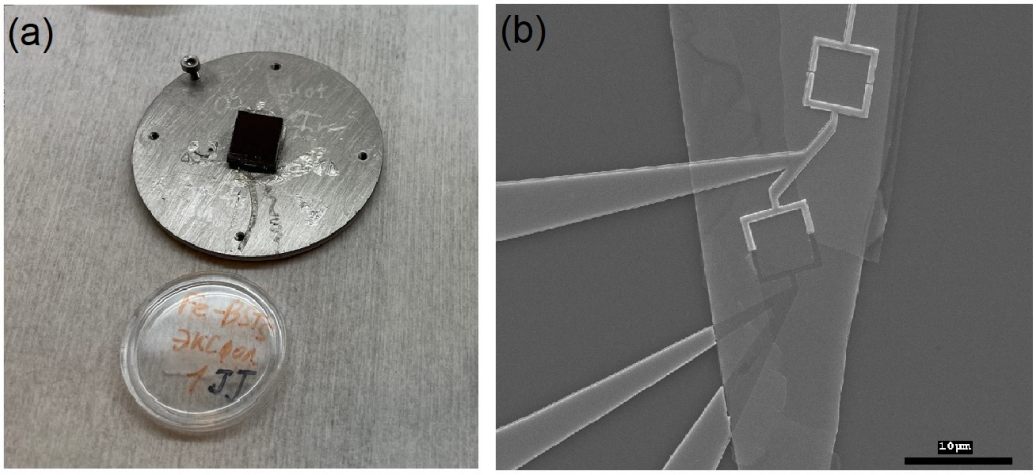

Figure 3.11: (a)Photo of the tilted table. (b) SEM-Image of the device after lift-off

lift-off. Part of the superconducting lead has removed with a few layers of the flake. To avoid such problems in the future, tests, which are described in the next paragraph, were performed.

3.7 Lift-off process

In order to work the technology of device fabrication out, tests with different thicknesses of the resist, thicknesses of the deposited niobium, and doses of electrons were performed.

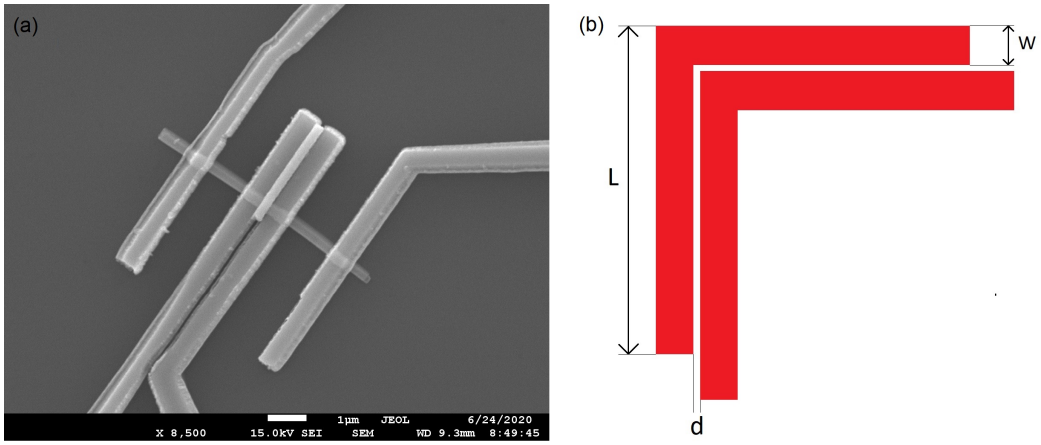

Figure 3.12: (a) SEM-Image of failed device. (b) Illustration of test-object. W=500 nm, $L = 5\ \mu m$, d is varied from 50 nm to 300 nm with 10 nm step.

Photo of the failed device is presented in Fig.3.12(a). One may see, that part of the gap between two superconducting leads has not removed during the lift-off process. We have fabricated test-objects (see Fig.3.12(b)) with varying distance between leads from 50 nm to 300 nm with 10 nm step to understand, at which distances there are no problems with lift-off and what is the real distance between the leads. The point is that, because of the overexposure, the distance between two leads is always smaller than in design.

Results of the test are presented in Fig.3.13. Clearly, if the thickness of the deposited material is small, we can fabricate smaller distances between Nb leads. For example, if we use 1 layer of PMMA A4 and deposit 50 nm of Nb, we can obtain a 65 nm gap between superconductors. But, sometimes flakes are thicker than 50 nm, hence we should use thicker metal films to prevent the formation of discontinuities at crystal boundaries, therefore, for the device, presented in this work, we used 2 layers of PMMA A4.

3.8 Cryogenic Transport Measurements

3.8.1 Dilution refrigerator

For transport measurements dilution refrigerator BlueFors LD-250 was used. Dilution refrigerators are systems that can provide continuous cooling power at temperatures below 300 mK. They can provide temperatures <10 mK and operate without moving parts at the low-temperature stages. A DR uses the heat of mixing of the two isotopes of helium, 3-He, and 4-He, to obtain cooling. In order to be able to run the dilution refrigerator's cooling

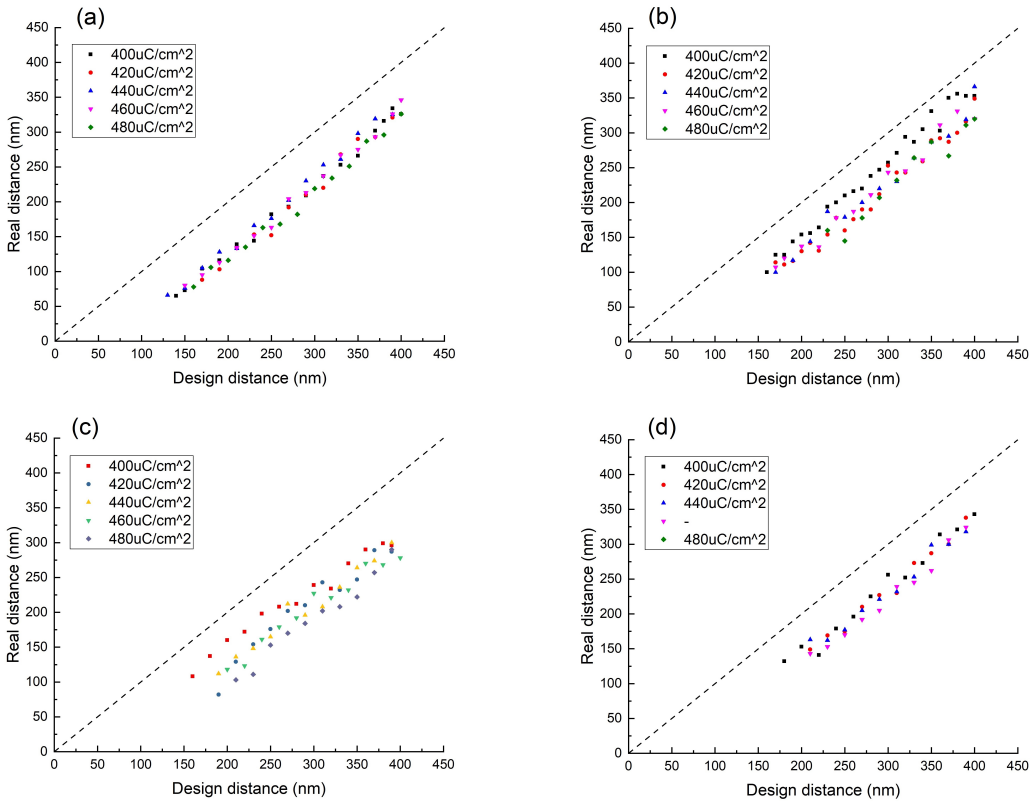

Figure 3.13: Results of tests for Josephson Junction fabrication for (a) 1 layer of resist and 50 nm of Nb, (b) 1 layer of resist and 100 nm of Nb, (c) 2 layers of resist and 100 nm of Nb, and (d) 2 layers of resist and 200 nm of Nb.

cycle, one should first obtain a starting temperature of about liquid helium (4.2 K) or below. In our system Pulse Tube cooler delivers low enough temperatures (about 4K) to start the DR cycle. After the DR is pre-cooled to <4.2 K, the 3-He/4-He mixture has to be condensed into the system. With a compressor, the pressure of the helium mixture is raised to about 2 bar. The heat exchangers in the incoming condensing line pre-cool the pressurized mixture to a low enough temperature for it to (partly) condense after the main flow impedance of the system.

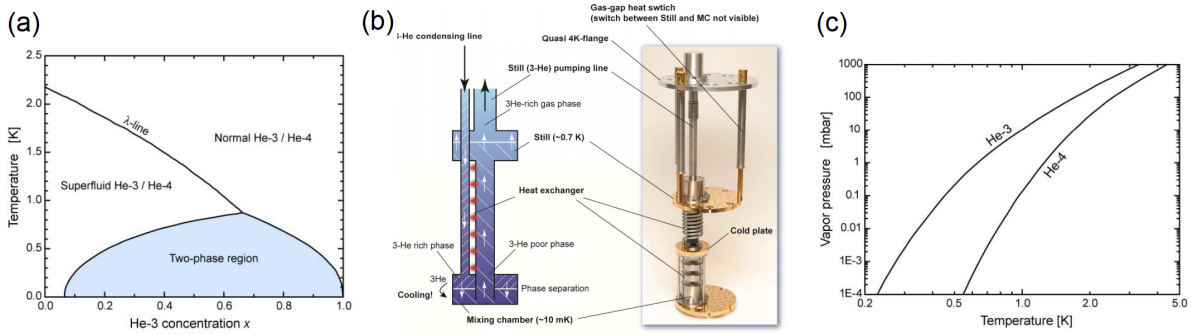

Figure 3.14: Principles of working of a dilution refrigerator. (a) Phase diagram of He-3/He-4 mixture.(b) Illustration of dilution unit. (c) Vapour pressure of He-3 and He-4 as a function of temperature.

After all mixture is condensed it makes up enough liquid to fill the mixing chamber, heat exchangers, and part of the still. The DR is now started by pumping the still. The helium pumped away from the still is returned into the system through the condensing line. Pumping the still will result in evaporative cooling, dropping its temperature to <0.8 K. The cooling cycle is possible due to the special properties of 3-He/4-He mixtures at low temperatures. At temperatures below 0.8 K (depending on concentration) the 3-He/4-He mixture will separate into two phases: a 3-He rich phase (concentrated phase) and a 3-He poor phase (dilute phase), as shown in 3.14(a). Approaching absolute zero temperature, the concentrated phase becomes pure 3-He while in the dilute 4-He rich phase there remains 6.4% of 3-He. The enthalpy of 3-He in the dilute phase is larger than in the concentrated phase. Therefore, some energy is required to take 3-He atoms from the concentrated phase and put them to the dilute phase. In a DR unit, this energy is taken from the mixing chamber, so cooling will occur. Because of gravity, the heavier 4-He rich phase will start to collect on the bottom of the mixing chamber. Eventually the dilute and concentrated phase will settle as shown in 3.14. In this state, the helium is pumped from the dilute phase of the still is almost pure 3-He, because the difference in vapor pressure between 4-He and 3-He is large (see 3.14). The 3-He is returned into the condensing line of the DR and precooled. In the mixing chamber, it is going through the phase boundary between dilute and concentrated phases, which results in the cooling of the MC. The osmotic pressure causes the 3-He in the dilute flow from the mixing chamber to return to the stationary one. In general, the performance of the dilution refrigerator is largely dependent on the efficiency of the countercurrent heat exchanger and the pumping system.

3.8.2 Ultra-sound bonding

After fabrication, the sample undergoes an ultrasonic bonding procedure, in which the contact pads of the measuring device are connected by thin aluminum wires to the contact pads on the sample holder (Fig.3.15). The principle of working of ultra-sound bonding is the following: machine applies same force between aluminum wire and pad and vibrates with ultra-sound frequency for a short period of time. It causes the melting of aluminum due to friction, creating good electrical contact. To protect the sample from static discharges during bonding and sample installation, all pads are connected to each other and grounded by the protective loop. This loop is removed after the sample is connected to the measuring set-up and grounded in another point.

3.8.3 Measurements set-up

For transport measurements, we used the so-called Keithley method (see Fig.3.16). In this method precision current source Keithley 6220 is used to apply bias current through the sample and nanovoltmeter Keithley 2182 is used to measure voltage drop on the sample. Sweeping current from point to point allows measuring I-V Characteristics. In "Results and

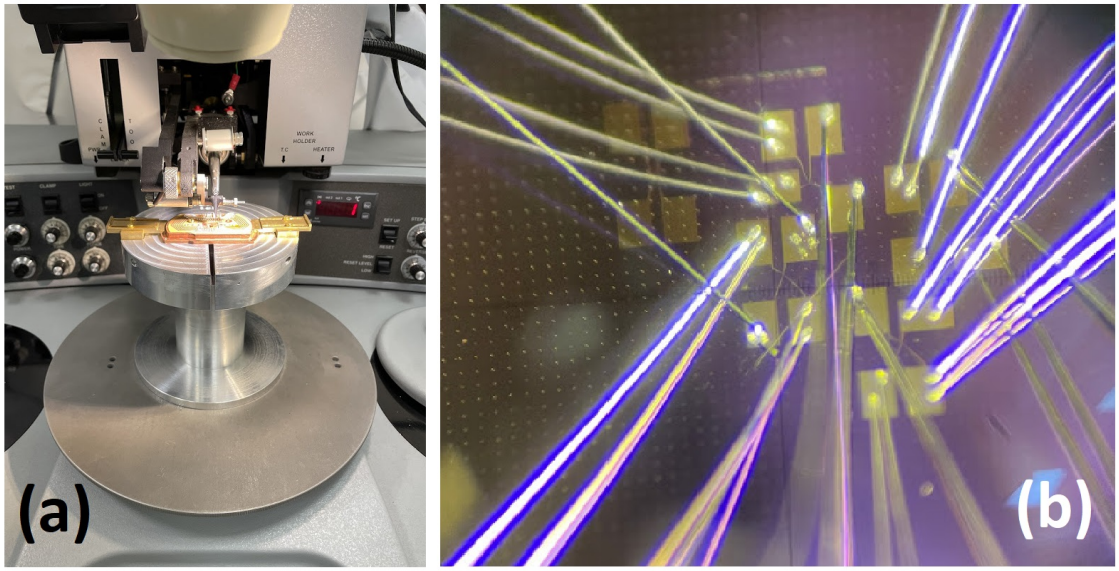

Figure 3.15: (a) Sample holder with the sample is located on the ultra-sound bonder. (b) Al wires connecting the sample and external measuring set-up.

Discussion" we plot dV/dI color plots. Differential resistance was calculated from smoothed I-V Curve (5 pts adjacent averaging) and then smoothed again with the same type of smoothing. In order to control the temperature of the sample LakeShore Resistance Bridge was used.

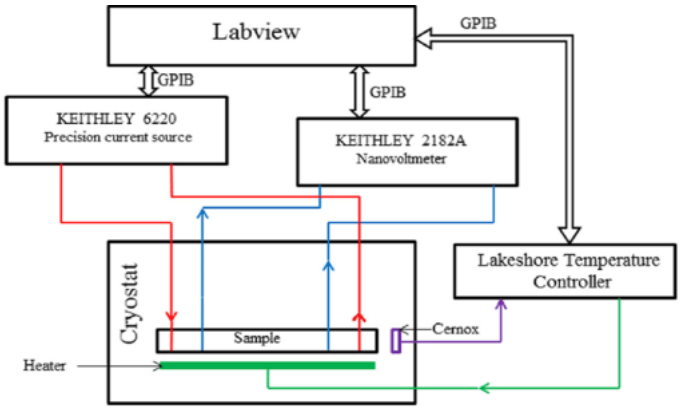

Figure 3.16: Sketch of the experimental setup. The figure is adapted from [24].

This instrument allows measuring the temperature of the sample via measuring the resistive thermometer and control temperature of the sample by PID-controlled heater, placed on the mixing chamber of the cryostat. The magnetic field was applied to the sample with help of a superconducting solenoid. Keithley 2400 was used to charge the solenoid. To combine all these instruments hand-made LabView program was used.

A very important aspect of low temperature measurements are the thermalization of electrons and noise reduction. The point is that at mK temperature electron-phonon interaction is very weak, hence the electronic temperature could be different from lattice temperature (bath temperature), which is measured by the resistive thermometer. But in

transport measurements to have low electronic temperature is very important, since electronic temperature determines all temperature-dependent transport effects, but not the bath temperature. In previous experiments in our laboratory another sample holder and filtering system were used. The sample holder was placed at the top of the MC plate and filtering system consisted of 2nd order RC filter with 17 kHz cut-off frequency (measured at room temperature) placed on a 1K plate and silver powder filter placed directly inside the sample holder. Details can be found in [25]. We have measured electronic temperature using a Coulomb blockade thermometer in this set-up. The result of measurements is presented in Fig.3.17(a). As one can see, at low temperatures electron temperature is higher than bath temperature and its minimum value is 100 mK.

For measurements, presented in this work, we firstly used the same RC-filter, but different sample holder without silver powder filter. The new sample holder is shown in Fig.3.17(c). It is a rotating sample holder connected to the MC plate of the cryostat. On the photo, one can see three boxes, on which the sample holder is mounted (the lower box is empty on the photo.). Thermalization of the sample holder is obtained through connecting the sample holder and Cu rod by Cu cable. Likely, the electronic temperature in this setup was even more, than presented in Fig.3.17(a). As a consequence, such a low critical current as few tens of nA is almost not distinguishable in I-V Curve (see Fig.3.17(b), green and black curves). We have found that decreasing the cut-off frequency to a few tenths of Hz greatly improves the quality of I-V Characteristic. It could indicate that we have additional source of noise in our set-up (ground loops, or instruments itself). We have not measured electron temperature with a new filter yet, but we are planning to reduce electron temperature down to base temperature in the nearest future by appropriate filtering set-up.

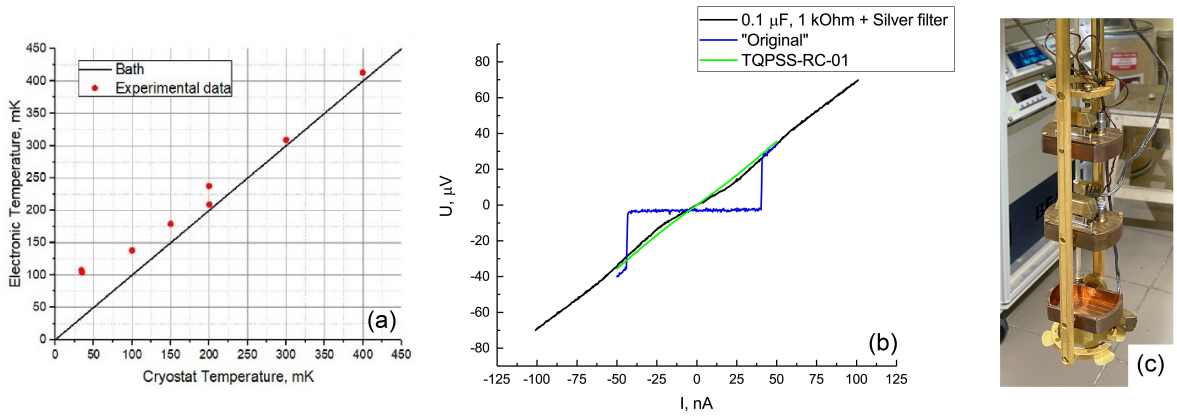

Figure 3.17: (a) Electronic temperature as a function of bath temperature, measured by Coulomb blockade thermometer. Red dots are experimental points, black line corresponds to the electronic temperature which is equal to the bath temperature. (b) I-V Characteristics of the device under study with different filters. Black and green curves correspond to the 2nd order RC-filter with a cut-off frequency of 17 kHz at room temperature, and blue one - 2 Hz at room temperature. (c) Photo of the sample holder.

Chapter 4

Results and Discussion

In this chapter, we present and analyze our experimental results. Firstly we performed Scanning Tunneling Microscopy and Angle-Resolved Photoemission Spectroscopy of bulk crystals. Further, we explored the transport properties of SQUID based on magnetic topological insulator Fe – $BiSbTe_2Se$.

4.1 Scanning Tunneling Microscopy

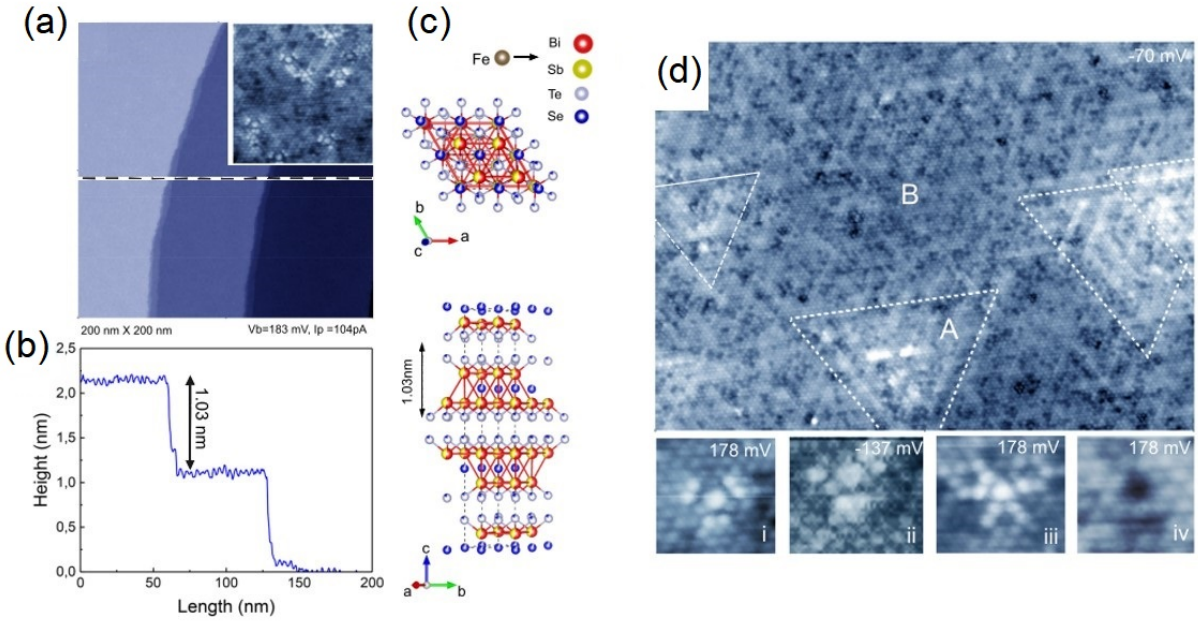

Figure 4.1: (a) A 200 nm × 200 nm STM image (bias voltage V_t = 183 mV and tunnel current I_t = 104 pA) of the *in situ* cleaved crystal. Atomically flat terraces are separated by 1.03 nm height steps, and the height of the terraces corresponds to QL. In the top-right inset, a 10 nm × 10 nm atomically resolved image with a typical set of defects. (b) The profile along the dashed line of the STM image. (c) The crystal structure of Fe-BSTS. The upper and bottom figures indicate the top view and the layered structure, respectively. The arrow indicates a single quintuple layer (QL). (d) A 10 nm × 10 nm atomically resolved image with a typical set of defects. i, ii, iii, iv, A and B corresponds to the tunneling spectra in Fig.4.2(a).

Owing to the excellent cleavage property of Fe-BSTS, sizable crystals were cleaved in the UHV chamber, and an atomically flat surface enabling STM/STS measurements was

obtained. STM mapping with a constant current of 104 pA and a bias voltage of 183 mV (Fig.4.1(a)) show clear atomically flat terraces. Interestingly, in Fig.4.1(a), one can see that steps consist of two steps. It is unlikely that we have a small region of not Se/Te terminated surface because it would mean that chemical bond breaking happens during mechanical exfoliation, which costs a lot of energy.

The observed step height was 1.03 nm, which corresponds to five atomic layers, the so-called quintuple layer (QL) of Fe-BSTS, as shown in Fig.4.1(b). These QLs are weakly bonded by van der Waals forces and terminated by chalcogen atoms (Se, Te). A local STM study of the flat terraces revealed well-ordered hexagonal lattices with randomly arranged atomic defects, reflecting its homogeneous substitution of (Bi, Sb, Fe) and (Te, Se) sites. The form of fingerprints depends on the type of defects and their depth in the QLs. (i),(ii),(iii) is hard to recognize, but (iv) is vacancy of Se/Te at the top layer [26].

Also, we have found big clusters of defects, which are shown by dashed triangular in the Fig.4.1(d). The origin of those is not known for now. For further analysis see Sections 4.2 and 4.3.

4.2 Scanning Tunneling Spectroscopy

Fig.4.2(a) shows tunnelling spectra at 4.2 K at different regions, corresponding to Fig.4.1(d). One can see that atomic defects (i), (ii) and (iii) slightly change the spectrum. Still, the spectrum in A and B are dramatically different, suggesting non-uniform properties of this material.

Fig.4.2(b) shows the averaged STS spectra measured at 4.2 K (blue line) and 77 K (red).

The rapid rise around $V_{bias} = -100$ mV and 300 mV corresponds to the bulk valence band (BVB) and bulk conduction band (BCB), respectively, and thus the bulk bandgap is $\Delta_{bulk} \approx 400$ meV (marked as a green-white gradient). The zero-bias voltage (Fermi energy E_F) is located close to the BVB, a hallmark of a p-type semiconductor. Within the bandgap, almost linear spectra appeared regardless of the measurement spots, which is a topologically protected feature and the linear band represents the surface states (the Dirac cone). The DP was estimated as $E_{DP} \sim -12$ meV from the extrapolation of the linear part of the spectra (see Fig.4.2(b)). Furthermore, the normalized spectrum of dI/dV (4.2 K) divided by the dI/dV (77 K) reveals some gap around the DP (see Fig.4.2(c)). Based on previous reports ($T_{Curri} < 50$ K) and other magnetically doped tetradymite systems ($T_{Curri} \sim 10$ K) the measurement temperatures should cross the Curie temperature of the present material and the observed gap represents the magnetic gap at the DP with a size of $\Delta_{mag} \approx 50$ meV, which is comparable to other magnetic TIs. We link the fact that the magnetic gap is partially filled in the region of the Dirac point because of the temperature fluctuations and the large number of atomic defects saturating the magnetic gap by electrons giving a nonzero background. The gap at the time- conserved DP is a hallmark of the broken time-

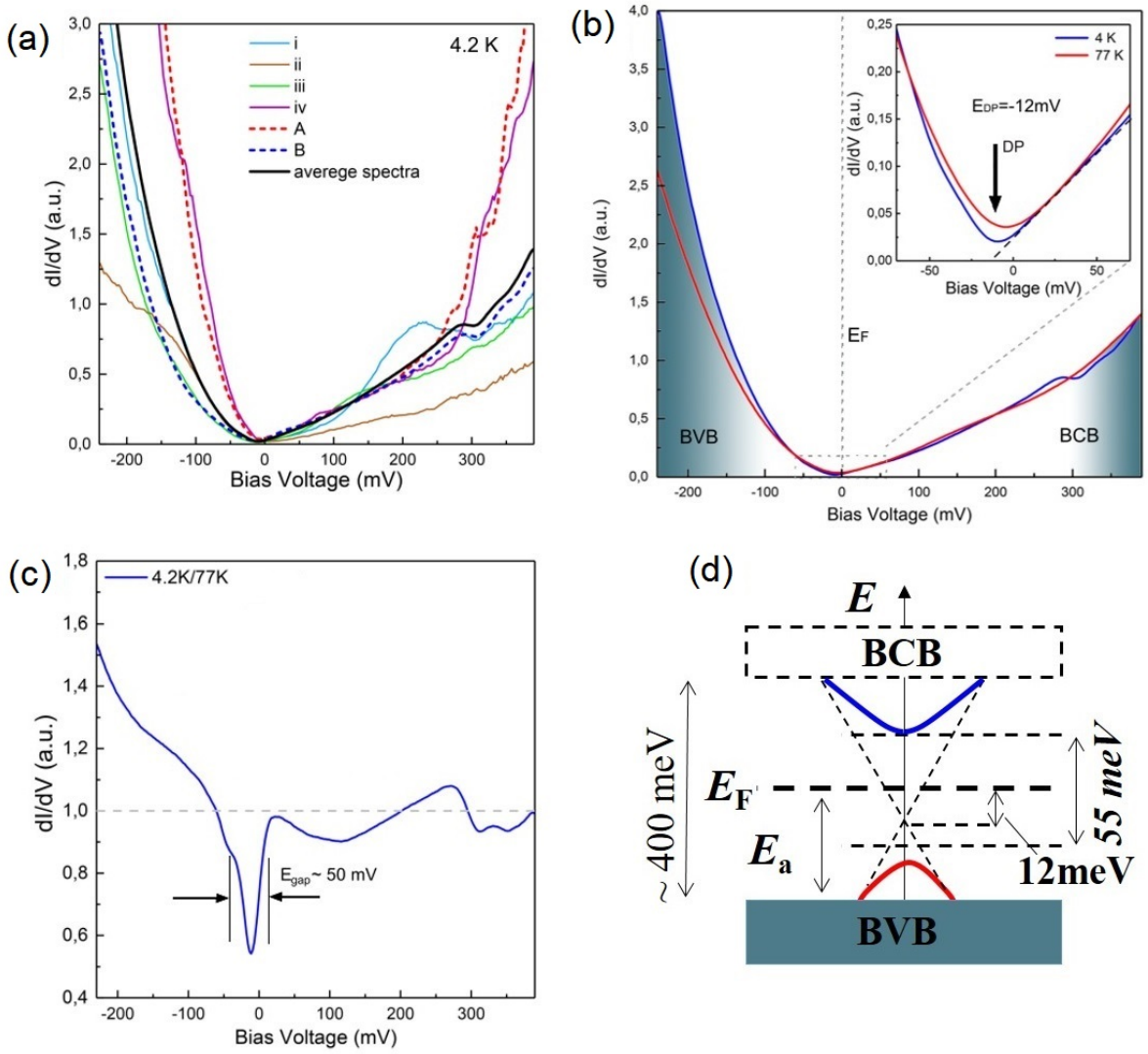

Figure 4.2: Results of Scanning Tunnelling Spectroscopy. (a) Tunneling spectra at 4.2 K at different regions. Corresponding regions are shown in Fig.4.1(d). (b) Average tunneling spectra at 4.2 K (blue line) and 77 K (red line). The inset shows a highlight around the zero-bias voltage. The dashed line represents a linear dispersion approximation, and the arrow indicates the estimated Dirac point at -12 mV. BVB and BCB are bulk valence and bulk conduction bands, respectively. (c) Normalized dI/dV spectrum of 4.2 K by the 77 K spectra. A clear 50 mV gap appears near the Dirac point. (d) Schematics of the band structure below Curie temperature, estimated from STS measurements.

reversal symmetry due to ferromagnetic ordering, whereas typical other origins, e.g., the Kondo effect, produce the gap structure at the E_F.

The Fig.4.2(d) shows the schematic band structure determined from the STS dI/dV spectra. The most prominent feature is that the location of the Fermi level is just above the DP and within the magnetic gap, which is an ideal situation to observe exotic magnetic gap-origin phenomena described in the introduction section.

4.3 Angle-resolved photoemission spectroscopy

In order to directly observe the magnetic gap at the Dirac point, we have conducted the ARPES measurements. Spectrum, taken at 20 K, is presented in Fig.4.3(a). Indeed, clear linear dispersion was observed and the Fermi level is slightly above the Dirac point, which is qualitatively consistent with the STS measurements and recent transport measurements (see Section 2). But quantitatively, ARPES shows that the Fermi level is higher than the Dirac point at 30 meV, which is more than we measured by STS.

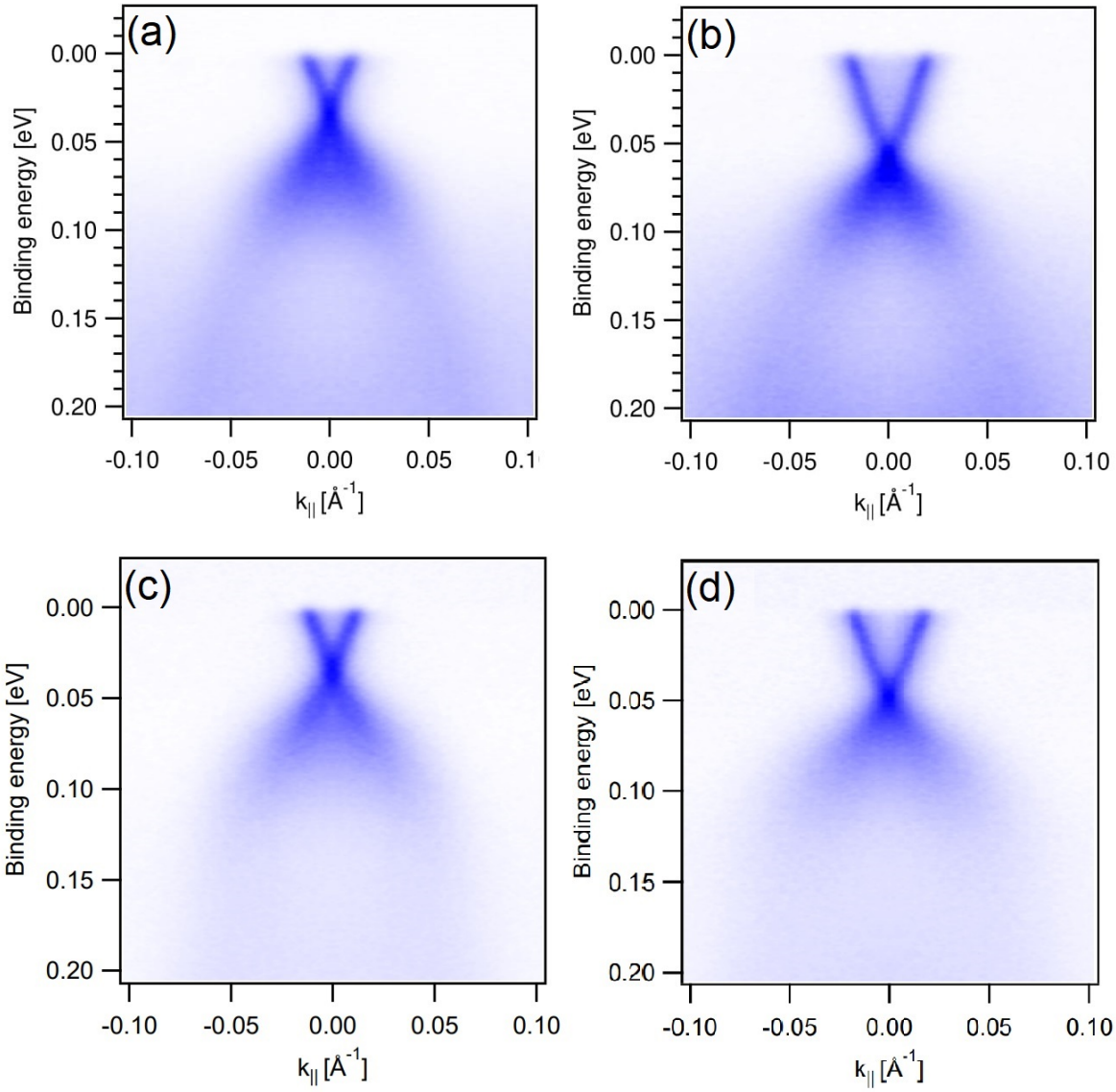

Figure 4.3: The intensity of photo-electrons as a function of Binding energy and wave-vector. (a) and (b) correspond to the spectrum from different spots on the same sample at 20K. (c) and (d) the same spots, but at 1.4K.

Moreover, the position of the Dirac point with respect to the Fermi level is varying a lot, depending on the spot on the sample. Fig.4.3(b) shows the spectrum from the same sample, but at another spot. And here, the Fermi level is higher than the Dirac point at 60

meV. This indicates the nonuniform electron doping in the material. This is consistent with the observation of finite density of states at the Dirac point by STS (inset of Fig.4.2(b)).

If we cool the sample down to 4.2 K, the gap at the Dirac point should open, according to STS measurements. But ARPES do not show magnetic gap even at 1.4 K temperature (see Fig.4.3(c) and (d)). We can suggest a few reasons to explain the absence of a gap in ARPES data:

1) Due to the big amount of point defects the position of the Dirac point varies more than the value of the magnetic gap and hence, in an integral signal of ARPES we do not see the gap because there is always the same finite density of states.

2) Nonuniform distribution of the Fe atoms in the sample. In that case, we can see the magnetization of the sample, but it could turn out that at the specific position of the X-Ray spot there are no Fe atoms and hence no magnetization and no gap.

4.4 Cryogenic transport measurements

In order to study induced superconductivity in Fe – $BiSbTe_2Se$ crystals, we have fabricated Superconducting Quantum Interferometer shown in Fig.4.4(a). The details of the device fabrication can be found in Chapter 3. The Current-Voltage characteristic at zero magnetic field and 14 mK is shown in Fig.4.4(b).

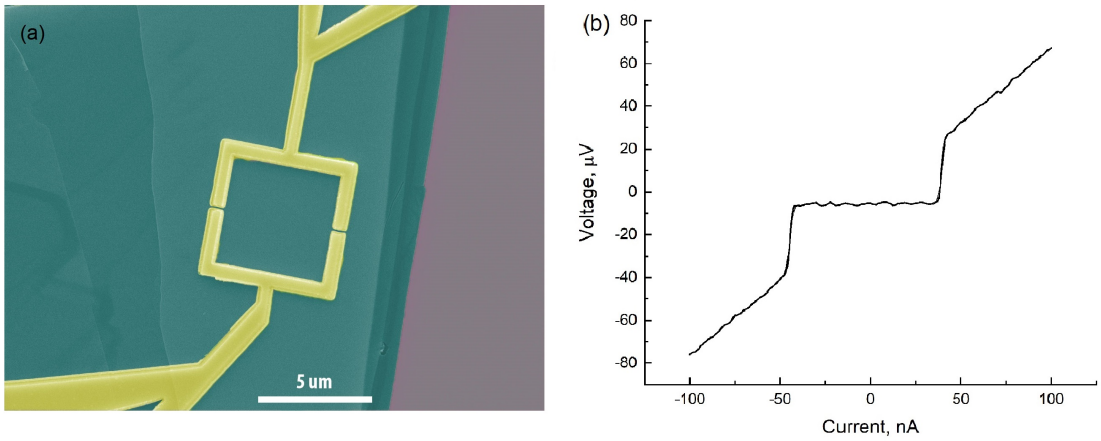

Figure 4.4: (a) False-collored SEM-Image of SQUID based on Fe-BSTS. Purple - Si/SiO_2 substrate, green - Fe-BSTS flake, yellow - Nb leads. (b) I/V Characteristic taken at H=0 G and T=14 mK.

If we apply an external magnetic field, the device is showing very pronounced coherent oscillations of the critical current (Fig.4.5). The period of these oscillations is consistent with the SQUID loop area:

$$\frac{\Phi_0}{\Delta H} = \frac{2.0678 \cdot 10^{-7}}{0.75}\ cm^2 = 27.57\ \mu m^2 \approx 5 \times 5\ \mu m^2, \tag{4.1}$$

where $\Phi_0 = \frac{h}{2e}$ is the superconducting flux quanta, ΔH is the period of the oscillations.

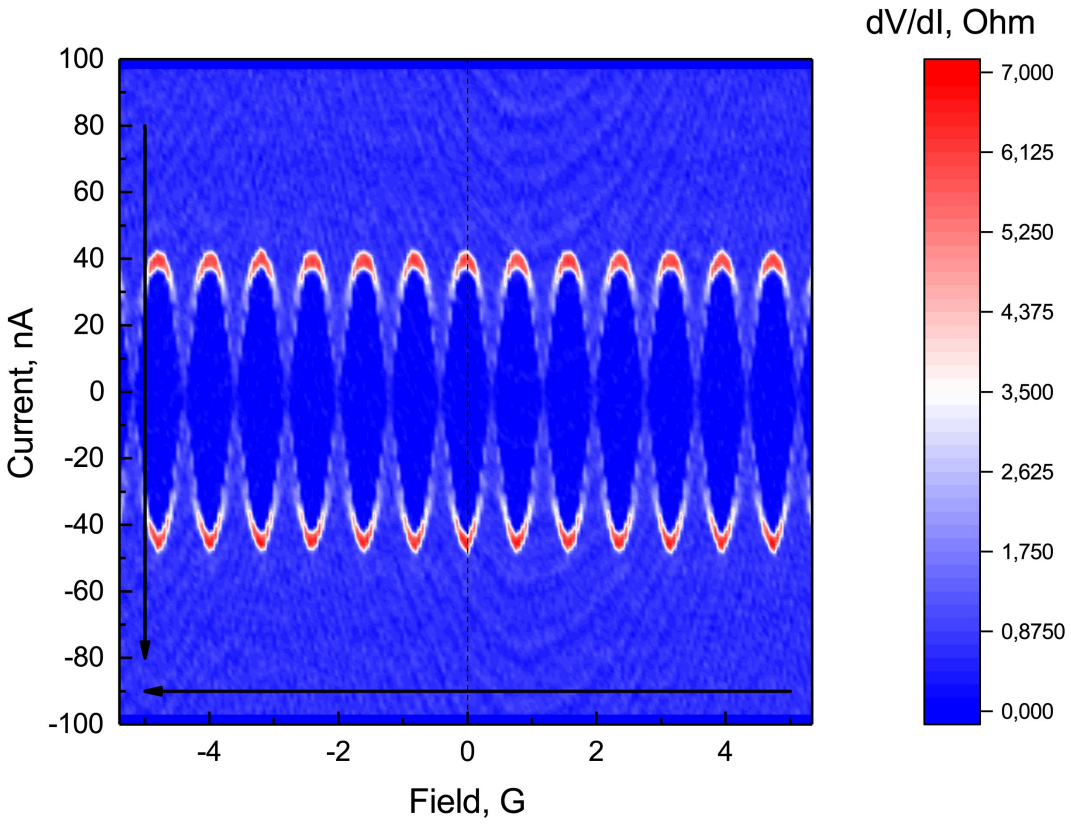

Figure 4.5: Color map of differential resistance as a function of Current and External Magnetic Field at T=20 mK. Arrows represent the direction of sweeping.

Notably, critical current drops to the zero value, which indicates that I_c of the left and the right Josephson Junctions are equal. Nevertheless, it should be noted that it is very hard to measure critical current as small as 5 nA since in this case, the Josephson energy E_J is the same order as the electronic temperature in our set-up (Fig.3.17 (a)):

$$E_J = \frac{I_c \Phi_0}{2\pi} = \frac{2.0678 \cdot 10^{-15} \cdot 5 \cdot 10^{-9}}{2 \cdot 3.14} \; J = 1.6463 \cdot 10^{-24} \; J \approx 100 \; mK, \tag{4.2}$$

where I_c is the critical current.

Fact that critical current drops to near-zero value is unexpected since in SEM-Image it is seen that the distance between superconducting leads are different and junctions are not symmetric. Reasons for that are analyzed below.

We can estimate the number of channels from the geometry of our junction:

$$N = \frac{W}{\lambda_F/2} = \frac{500}{30/2} \approx 30, \tag{4.3}$$

where W is the width of the Josephson junction, determined from SEM-Image, and λ_F is

the Fermi wavelength, determined from the ARPES spectra.

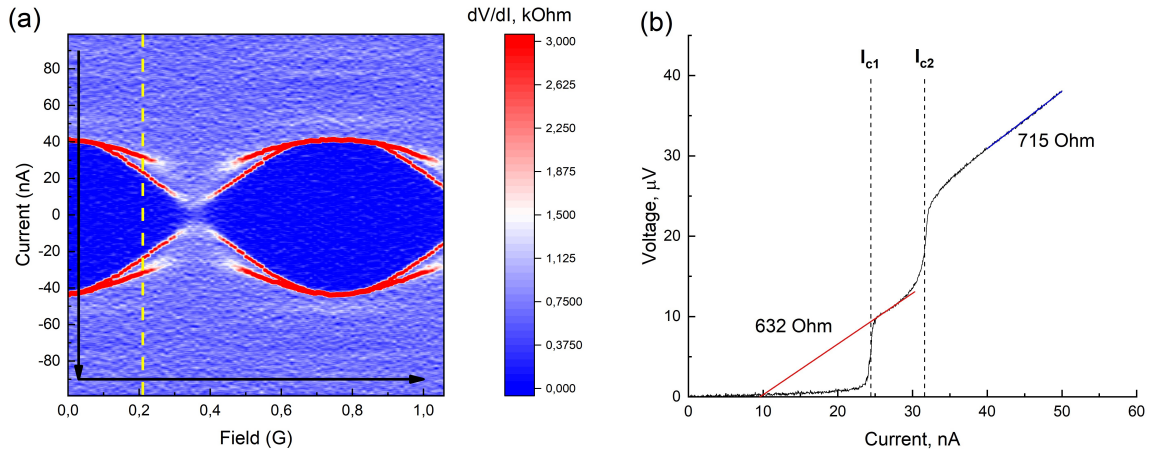

Figure 4.6: (a) Color map of differential resistance as a function of Current and External Magnetic Field at T=20 mK. Arrows represent the direction of sweeping. (b) I/V Characteristics taken at H=0.21 G and T=20 mK (yellow dashed line in (a)). Dashed lines indicate I_{c1} and I_{c2} and red and blue lines are linear fits after the first and the second critical current, respectively. Numbers correspond to the slope of the lines.

Also, we can estimate the number of conductive channels from the normal resistance, assuming that the interface between a superconductor and a topological insulator is transparent:

$$N_{cond} = \frac{e^2/h}{R_N} = \frac{25812}{825} \approx 31, \tag{4.4}$$

where R_N is the normal resistance at higher currents (see Fig.4.8(b)). Those two values are consistent with each other. Nevertheless, as we will see next, not all of them are carrying supercurrent.

Another notable feature of this device is what we call "double critical current", which can be seen if we zoom in the region where the critical current goes to zero (see Fig.4.6(a)). So, there is a separation of critical current I_c to I_{c1} and I_{c2} at some fields. I-V Characteristics of SQUID taken at H=0.21 G is presented in Fig.4.6(b). Two clear steps are seen, accompanied by the change in normal resistance from 632 Ohm to 715 Ohm.

In high fields, instead of the standard modulation of the critical current by the Fraunhofer dependence, a monotonic decrease of the critical current is observed. It suggests that we are in the narrow junction limit, and the magnetic field acts on Cooper pairs by breaking the mechanism. At a certain value of the magnetic field, two critical currents split completely, as shown in Fig.4.7(a) and (b). The temperature dependence of critical currents is shown in Fig.4.8(a). It can be seen that the critical current increases with decreasing temperature linearly, but at a temperature of 0.4 K the critical current I_{c1} is becoming limited by the critical current I_{c2}. The linear course of the temperature dependence is consistent with the ballistic nature of the transport with a transparent interface, which is also supported by the

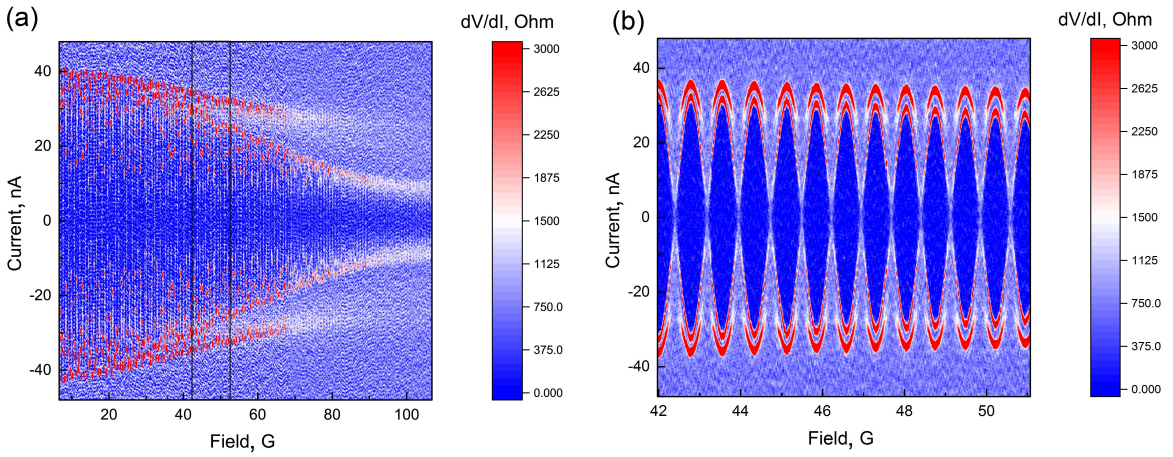

Figure 4.7: Color maps of differential resistance as a function of Current and External Magnetic Field at T=20 mK. (b) is the zoom of the region on (a), highlighted with a black rectangle.

observation of excess current (see Fig.4.8(b)).

From the critical temperature of SQUID we can estimate the proximity induced gap:

$$\Delta = 1.76 k_B T_c = 1.76 \cdot 8.6 \cdot 10^{-5} \cdot 1.69 = 0.25\ meV, \tag{4.5}$$

where T_c is the critical temperature of the SQUID and k_B is the Boltzmann constant. Of course, there is no evidence, that BCS theory works in such systems since it is predicted that p-wave superconductivity should exist in proximitized surface states of topological insulators. Nevertheless, measurements on similar systems show an induced gap of the same value.

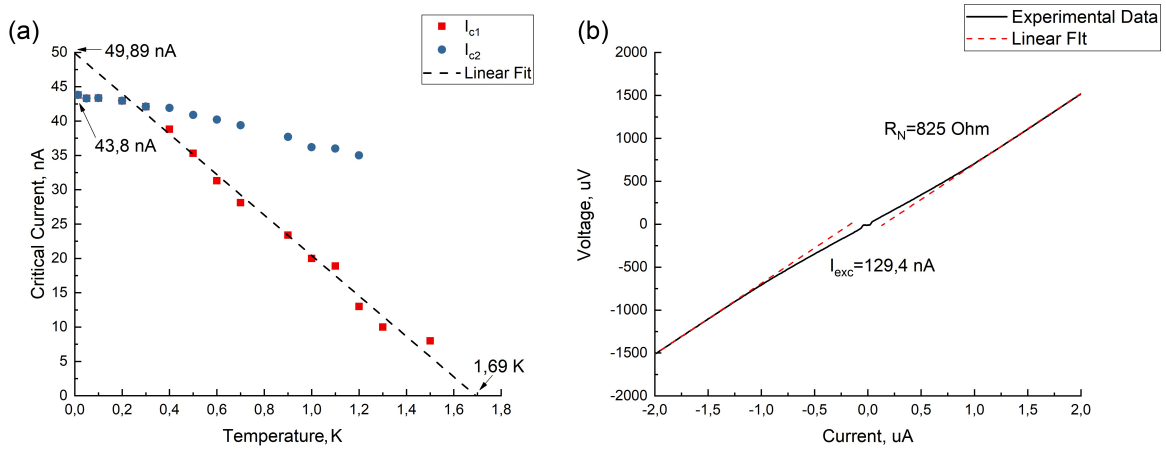

Figure 4.8: (a) Temperature dependence of the critical currents I_{c1} and I_{c2} at zero magnetic field. The dashed line corresponds to the linear fit of I_{c1}. (b) I/V Characteristic taken at H=0 G and T=26 mK. Red dashed lines are linear fits of the high-voltage regions. Numbers correspond to the slope of lines and the intersect with Current axis.

Knowing the value of gap allows us to estimate the current, which is flowing through

single conductive channel:

$$I_Q = \frac{e\Delta}{2\hbar} = \frac{0.25 \cdot 10^{-3} \cdot 1.6 \cdot 10^{-19}}{6.58 \cdot 10^{-16}}\ nA = 30.35\ nA. \tag{4.6}$$

Interestingly, this value is nicely co-inside with the critical current of a single Josephson junction in our SQUID $I_c = \frac{49.89}{2}\ nA = 24.945\ nA$, so, we can conclude that out of 30 channels, only a few of them are coherent. That explains symmetry of SQUID: variation in distance between superconducting leads doesn't matter since we are in the ballistic regime, and variation in the width of superconducting leads doesn't matter since there are only a few coherent channels at each Josephson junction.

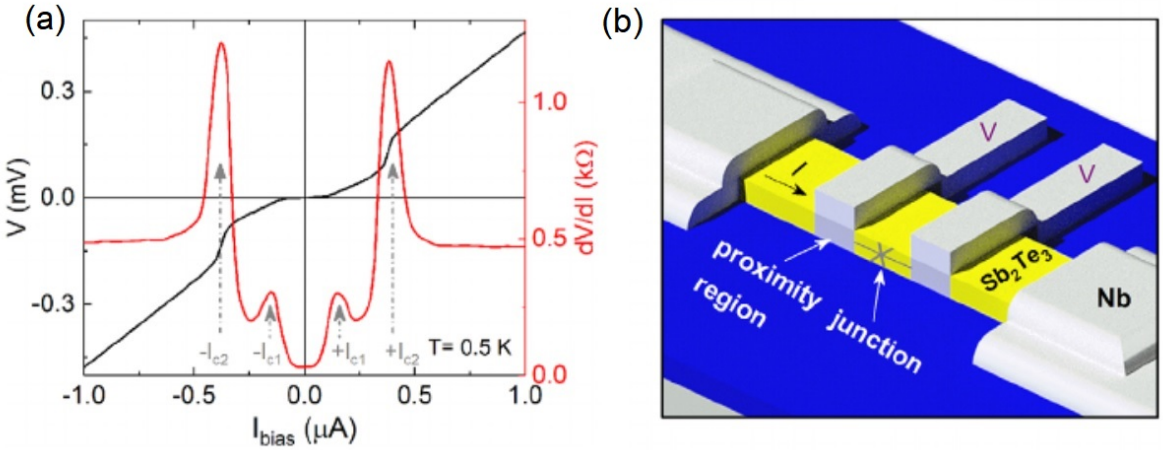

Figure 4.9: (a) I–V characteristic and dV/dI of a Sb_2Te_3-based Josephson junction. (b) Schematic illustration of a proximity induced superconducting areas underneath the Nb electrodes. Figure is adopted from [27]

That double critical current feature is frequently observed in Josephson junctions based on different topological insulators or Dirac semi-metal flakes. For example, in [27], Zhang et al. observed similar behavior, which is presented in Fig.4.9. One of the possible explanations of the "double critical current" feature is that we have two Josephson junctions in series. The trivial explanation would be that the second weak link emerges at the boundary of the flake. But this is inconsistent with the fact, that the second critical current also oscillates and the period of oscillation is corresponds to the area of the SQUID. Plus, we have a 4-probe measurement, and potential and current contacts are separated on the surface of the crystal, so, even if we had a weak link in the boundary of the crystal, we would not measure it. Thus, likely, there is another week link underneath the Nb contacts near Josephson junction. That's why the second critical current is limiting the first critical current, which can be seen in Fig4.6(a) and also why we have the same period of oscillations of the $I_{c2}(H)$. We believe that some dirty region might form between Nb and flake due to the Ar plasma cleaning and Nb deposition. This hypothesis needs to be confirmed.

Chapter 5
Conclusion and Future Work

During my MSc project, I have studied a lot of literature on topological phases of matter and got a lot of experience with experimental work on sample preparation and cryogenic measurements. Now I came close to understand what we should do to measure the topological properties, including the search for Majorana fermions.

In particular, in the frame of scientific work, the local electronic properties of Fe-BSTS have been studied by STM/STS and ARPES. Were demonstrated that the Fermi energy position inside the bulk bandgap makes this material a real bulk insulator. In addition, the signatures of the magnetic gap present were observed by STS. Still, independent ARPES measurement did not resolve any magnetic gap near the Dirac point in the surface states, probably due to the inhomogeneous distribution of the iron atoms, which is supported by observing the defect clusters on the surface topography image.

Also, were demonstrated the ballistic Josephson effect on Fe-BSTS. Fe-BSTS based dc-nanoSQUID showed very pronounced oscillations of critical current vs an external magnetic field. Critical current drops to zero due to supercurrent is flowing through the limited quantity coherent ballistic channels. Another feature was observed is the double-critical current. We supposed that the second critical current originates from the region underneath the Nb leads formed during Ar plasma etching and Nb deposition.

To realise the project, several methods and technologies have been studied. In particular: STM/STS, ARPES studies; exfoliation and device fabrication of the superconducting hybrid structures based on magnetic topological insulator flakes has been worked out; using e-beam lithography and magnetron sputtering technique formed Nb contact was sputtered on top of exfoliated crystals; the cryogenic part of the dilution refrigerator was prepared for studies of such kind of devices.

In the nearest future, we plan to conduct Transmission Electron Microscopy (TEM) of this device to test the hypotheses about the extra superconducting region under the Nb leads. Also, to study chiral Majorana physics, it is necessary to prove the inhomogeneity of iron atoms and resolve this issue by optimizing crystal growth.

Now I am really interested in continuing research in this field as a PhD student.

Bibliography

[1] Zhang H., Liu C.-X., Qi X.-L., Dai X., Fang Z., and Zhang S.-C. Topological insulators in bi_2se_3, bi_2te_3 and sb_2te_3 with a single dirac cone on the surface. *Nature Physics*, 5(6):438–442, 2009.

[2] Bo Zhou, Liu Z. K., J. G. Analytis, K. Igarashi, S. K. Mo, D. H. Lu, R. G. Moore, I. R. Fisher, T. Sasagawa, Z. X. Shen, Z. Hussain, and Y. L. Chen. Controlling the carriers of topological insulators by bulk and surface doping. *Semicond. Sci. Technol.*, 27, 2012.

[3] Chandra Shekhar, C. E. ViolBarbosa, Binghai Yan, Siham Ouardi, W. Schnelle, Gerhard H. Fecher, and Claudia Felser. Evidence of surface transport and weak antilocalization in a single crystal of the bi_2te_2Se topological insulator. *Phys. Rev. B*, 90:165140, Oct 2014.

[4] Y. Tokura, K. Yasuda, and A. Tsukazaki. Magnetic topological insulators. *Nature Reviews Physics*, 1:126–143, 2019.

[5] Y. L. Chen, J.-H. Chu, J. G. Analytis, Z. K. Liu, K. Igarashi, H.-H. Kuo, X. L. Qi, S. K. Mo, R. G. Moore, M Lu, D. H. and. Hashimoto, T. Sasagawa, S. C. Zhang, I. R. Fisher, Z. Hussain, and Shen Z. X. Massive dirac fermion on the surface of a magnetically doped topological insulator. *Science*, 329:659–662, 2010.

[6] Cui-Zu Chang, Jinsong Zhang, Xiao Feng, Jie Shen, Zuocheng Zhang, Minghua Guo, Kang Li, Yunbo Ou, and et al. Experimental observation of the quantum anomalous hall effect in a magnetic topological insulator cui-zu. *Science*, 340:167–170, 2013.

[7] L. Pan, X. Liu, Q.L. He, A. Stern, G. Yin, X. Che, Q. Shao, P. Zhang, P. Deng, C.-Y. Yang, B. Casas, E.S. Choi, J. Xia, X. Kou, and K.L. Wang. Probing the low-temperature limit of the quantum anomalous hall effect. *Science Advances*, 6, 2020.

[8] T. Arakane, T. Sato, S. Souma, K. Kosaka, K. Nakayama, M. Komatsu, T. Takahashi, Z. Ren, K. Segawa, and Y. Ando. Tunable dirac cone in the topological insulator $bi_{2-x}sb_xte_{3-y}se_y$. *Nature Communications*, 3, 2012.

[9] R. Yano, H.T. Hirose, K. Tsumura, S. Yamamoto, M. Koyanagi, M. Kanou, H. Kashiwaya, T. Sasagawa, and S. Kashiwaya. Proximity-induced superconducting states of magnetically doped 3d topological insulators with high bulk insulation. *Condensed Matter*, 4, 2019.

[10] R. Yano, A. Kudriashov, H.T. Hirose, T. Tsuda, H. Kashiwaya, T. Sasagawa, A.A. Golubov, V.S. Stolyarov, and S. Kashiwaya. Magnetic gap of fe-doped $bisbte_2se$ bulk single crystals detected by tunneling spectroscopy and gate-controlled transports. *Journal of Physical Chemistry Letters*, 12:4180–4186, 2021.

[11] E. Majorana. Teoria simmetrica dell'elettrone e del positrone. *Nuovo Cimento*, 14:1924–1942, 1937.

[12] Y. E. Kraus, A. Auerbach, H.A. Fertig, and S.H. Simon. Testing for majorana zero modes in a $p_x + ip_y$ superconductor at high temperature by tunneling spectroscopy. *Phys. Rev. Lett.*, 101, 2008.

[13] L Fu and C.L. Kane. Superconducting proximity effect and majorana fermions at the surface of a topological insulator. *Phys. Rev. Lett.*, 100, 2008.

[14] J. Alicea, Y. Oreg, G. Refael, F. Oppen, and Matthew P. A. Fisher. Non-abelian statistics and topological quantum information processing in 1d wire networks. *Nature Physics*, 7:412–417, 2011.

[15] Qing Lin He, Lei Pan, Alexander L Stern, Edward C Burks, Xiaoyu Che, Gen Yin, Jing Wang, Biao Lian, Quan Zhou, Eun Sang Choi, Koichi Murata, Xufeng Kou, Zhijie Chen, Tianxiao Nie, Qiming Shao, Yabin Fan, Shou Cheng Zhang, Kai Liu, Jing Xia, and Kang L Wang. Chiral Majorana fermion modes in a quantum anomalous Hall insulator–superconductor structure. *Science*, 357(6348):294–299, 2017.

[16] Biao Lian, Xiao-Qi Sun, Abolhassan Vaezi, Xiao-Liang Qi, and Shou-Cheng Zhang. Topological quantum computation based on chiral majorana fermions. *Proceedings of the National Academy of Sciences*, 115(43):10938–10942, 2018.

[17] Jing Wang, Quan Zhou, Biao Lian, and Shou-Cheng Zhang. Chiral topological superconductor and half-integer conductance plateau from quantum anomalous hall plateau transition. *Phys. Rev. B*, 92:064520, Aug 2015.

[18] Morteza Kayyalha, Aleksandr Kazakov, Ireneusz Miotkowski, Sergei Khlebnikov, Leonid P. Rokhinson, and Yong P. Chen. Highly skewed current–phase relation in superconductor–topological insulator–superconductor Josephson junctions. *npj Quantum Materials*, 5(1), 2020.

[19] Chang-An Li, Jian Li, and Shun-Qing Shen. Majorana-josephson interferometer. *Phys. Rev. B*, 99:100504, Mar 2019.

[20] J. Kaas. Scanning tunneling microscopy and spectroscopy of iron pnictide superconductors.(master's thesis)., 2010.

[21] K. McElroy. Scanning tunneling microscopy studies in both real- and momentum-space of the doping dependence of cuprate electronic structure.(phd thesis)., 2005.

[22] https://mipt.ru/upload/medialibrary/433/astrakhantsevadiplommfti.pdf.

[23] S.V. Borisenko, V.B. Zabolotnyy, A.A. Kordyuk, D.V. Evtushinsky, T.K. Kim, E. Carleschi, B.P. Doyle, R. Fittipaldi, M. Cuoco, A. Vecchione, and H. Berger. Angle-resolved photoemission spectroscopy at ultra-low temperatures. *Journal of visualized experiments*, 68, 2012.

[24] Pankaj Sagar and R. Karunanithi. A non-contact rrr estimation using planar inductor sensing element. *Measurement*, 146:758–769, 07 2019.

[25] https://istina.msu.ru/diplomas/162659229/.

[26] Asteriona-Maria Netsou, Dmitry A. Muzychenko, Heleen Dausy, Taishi Chen, Fengqi Song, Koen Schouteden, Margriet J. Van Bael, and Chris Van Haesendonck. Identifying native point defects in the topological insulator bi2te3. *ACS Nano*, 14(10):13172–13179, 2020.

[27] Jinzhong Zhang, Abdur Rehman Jalil, Pok-Lam Tse, Jonas Kölzer, Daniel Rosenbach, Helen Valencia, Martina Luysberg, Martin Mikulics, Gregory Panaitov, Detlev Grützmacher, Zhigao Hu, Jia Grace Lu, and Thomas Schäpers. Proximity-effect-induced superconductivity in nb/sb2te3-nanoribbon/nb junctions. *Annalen der Physik*, 532(8):2000273, 2020.